

Article

Power Production, Inter- and Intra-Array Wake Losses from the U.S. East Coast Offshore Wind Energy Lease Areas

Sara C. Pryor ^{1,*}  and Rebecca J. Barthelmie ² ¹ Department of Earth and Atmospheric Sciences, Cornell University, Ithaca, NY 14853, USA² Sibley School of Mechanical and Aerospace Engineering, Cornell University, Ithaca, NY 14853, USA; rb737@cornell.edu

* Correspondence: sp2279@cornell.edu; Tel.: +1-607-255-3376

Abstract: There is an urgent need to develop accurate predictions of power production, wake losses and array–array interactions from multi-GW offshore wind farms in order to enable developments that maximize power benefits, minimize levelized cost of energy and reduce investment uncertainty. New, climatologically representative simulations with the Weather Research and Forecasting (WRF) model are presented and analyzed to address these research needs with a specific focus on offshore wind energy lease areas along the U.S. east coast. These, uniquely detailed, simulations are designed to quantify important sources of wake-loss projection uncertainty. They sample across different wind turbine deployment scenarios and thus span the range of plausible installed capacity densities (ICDs) and also include two wind farm parameterizations (WFPs; Fitch and explicit wake parameterization (EWP)) and consider the precise WRF model release used. System-wide mean capacity factors for ICDs of 3.5 to 6.0 MWkm⁻² range from 39 to 45% based on output from Fitch and 50 to 55% from EWP. Wake losses are 27–37% (Fitch) and 11–19% (EWP). The discrepancy in CF and wake losses from the two WFPs derives from two linked effects. First, EWP generates a weaker ‘deep array effect’ within the largest wind farm cluster (area of 3675 km²), though both parameterizations indicate substantial within-array wake losses. If 15 MW wind turbines are deployed at an ICD of 6 MWkm⁻² the most heavily waked wind turbines generate an average of only 32–35% of the power of those that experience the freestream (undisturbed) flow. Nevertheless, there is no evidence for saturation of the resource. The wind power density (electrical power generation per unit of surface area) increases with ICD and lies between 2 and 3 Wm⁻². Second, EWP also systematically generates smaller whole wind farm wakes. Sampling across all offshore wind energy lease areas and the range of ICD considered, the whole wind farm wake extent for a velocity deficit of 5% is 1.18 to 1.38 times larger in simulations with Fitch. Over three-quarters of the variability in normalized wake extents is attributable to variations in freestream wind speeds, turbulent kinetic energy and boundary layer depth. These dependencies on meteorological parameters allow for the development of computationally efficient emulators of wake extents from Fitch and EWP.



Citation: Pryor, S.C.; Barthelmie, R.J. Power Production, Inter- and Intra-Array Wake Losses from the U.S. East Coast Offshore Wind Energy Lease Areas. *Energies* **2024**, *17*, 1063. <https://doi.org/10.3390/en17051063>

Academic Editors: Alberto Troccoli and Laurent Dubus

Received: 15 December 2023

Revised: 5 February 2024

Accepted: 21 February 2024

Published: 23 February 2024

Keywords: wind turbines; mesoscale model; WRF; wake modeling; array–array interactions; Fitch; EWP; capacity factors; wake extent; ‘deep array effect’



Copyright: © 2024 by the authors. Licensee MDPI, Basel, Switzerland. This article is an open access article distributed under the terms and conditions of the Creative Commons Attribution (CC BY) license (<https://creativecommons.org/licenses/by/4.0/>).

1. Introduction

1.1. Growth of Offshore Wind Energy Installed Capacity

Offshore wind energy is widely recognized as having a key role to play in meeting global, national and regional goals for reducing emission of radiatively active (greenhouse) gases [1], and a number of nations are now investing in harnessing offshore wind resources [2,3]. Excluding recent challenges related to global inflation and supply chains [4], the levelized cost of energy (LCoE) for electricity generated by wind turbines deployed offshore has historically exhibited marked declines [5]. Pre-construction estimates of project costs in mature markets are becoming increasingly accurate [6]. An analysis by the Global

Wind Energy Council (GWEC) indicates that offshore wind using fixed-bottom foundations has become the third most cost-competitive electrical generation technology after onshore wind and solar photovoltaics [3].

The world's first offshore wind farm was installed in the coastal waters of Denmark and commenced operation in 1991 [7]. It comprised 11 Bonus 450 kW wind turbines, for a total installed capacity (IC) of less than 5 MW [7]. At the end of 2020, 6600 wind turbines were deployed in European waters in over 112 wind farms [5]. Data from the GWEC indicate 6.6 GW of new IC was added during 2022, taking the global offshore IC to 64.3 GW [3].

While Europe has a long history of deploying wind turbines offshore [8,9], China commissioned its first offshore wind project in 2010. Nevertheless, Chinese offshore wind IC has subsequently risen rapidly [3] and in 2022 Asia-Pacific overtook Europe as the region with the highest offshore IC [3]. The large offshore wind resource possessed by the United States of America (U.S.) [10–12] has until recently remained untapped [13]. Efforts to harness these resources, particularly along the U.S. east coast, are now being actively pursued [14,15]. Access to offshore wind resources between 3 and 200 miles from the U.S. coastline is managed and regulated by the U.S. federal government [2]. Major auctions of offshore wind energy lease areas (LAs) along the U.S. east coast have been offered by the Bureau of Ocean Energy Management (BOEM) which is an agency within the U.S. Department of the Interior. The pipeline of offshore wind energy projects in the U.S. is >40 GW of installed capacity [16]. GWEC global projections are for IC additions within the next decade (2023–2032) of >390 GW [3]. Europe alone (excluding the UK) has targets to expand offshore wind installed capacity by ≥ 60 GW by 2030 and ≥ 300 GW by 2050 [3].

Given the low water depth areas that can support bottom-mounted wind turbines are finite, it is inevitable that at least some of the offshore wind energy capacity additions will be in wind farms that are subject to wakes from other offshore wind turbine arrays [17]. Coordination of lease area identification and wind farm development and potentially even coordinated operation of offshore wind farms may aid in maximizing system-wide power output by avoiding excess wake-induced power losses and reducing the potential for legal disputes [18–20].

A range of policies have been employed by different countries to stimulate and enable expansion of the offshore wind energy industry [21]. Many have focused on leasing of development areas in federal waters and production tax credits. Specific to the U.S., the 2022 Inflation Reduction Act provides increased Renewable Electricity Production Tax Credit (PTC) and Business Energy Investment Tax Credit (ITC) for wind energy projects that commence construction by the end of 2024 (information sheet: 'Advancing the Growth of the U.S. Wind Industry: Federal Incentives, Funding, and Partnership Opportunities' available for download from: <https://www.energy.gov/sites/default/files/2023-02/weto-funding-fact-sheet-feb-23.pdf> Accessed on 1 November 2023).

The levelized cost of energy (LCoE) from offshore wind farms is determined by the annual energy production (AEP), that is the amount of electricity generated by the wind turbines, plus factors such as capital expenditures, operating expenditures and discounting rate in addition to the availability of subsidies [22]. AEP is determined principally by the wind resource and is reduced when increasing numbers of wind turbines operate in the wake of upstream wind turbines/wind farms and thus experience lower inflow wind speeds. The cost of capital for prospective offshore wind energy projects, the price risk and ability to obtain support for a project depend on multiple factors including the confidence associated with projected AEP (and the variability therein) [23–25]. These factors are thus contingent upon the confidence with which wake-induced reductions in AEP (power losses) can be specified. This, coupled with trends described in more detail in Section 1.2, provide clear motivation to better quantify expected power production from, and wake-induced power losses within and between, the new generation of larger offshore wind farms.

1.2. Trends in Offshore Wind Energy

The increase in offshore wind energy installed capacity is being primarily driven by three factors: (i) Increased number of wind turbine arrays [3]. (ii) Increased number of wind turbines being deployed in each array [5,26]. (iii) Increase in the physical dimensions and rated power of wind turbines [3]. The mean IC of European offshore wind farms doubled from 321 MW to 621 MW between 2010 and 2019 [26] but continued to employ wind turbine spacing of 4 to 11 rotor diameters (D) with a mean of 7.7 D [27] yielding typical installed capacity densities (ICDs, i.e., rated power of the installed wind turbines per square kilometer of ground) of 2.5 to 12 MWkm⁻² [28].

The largest currently operating offshore wind array is Hornsea 2 located about 90 km east of the UK coast in the North Sea. This project became fully operation in summer 2022 (<https://hornseaprojects.co.uk/hornsea-project-two> Accessed on 1 November 2023). It has a total IC of over 1.3 GW and comprises 165 wind turbines within a deployment area of 462 km². The second largest is Hornsea 1 which has an installed capacity of 1.2 GW over an area of 407 km² and commenced operation in December 2019 (<https://hornseaprojects.co.uk/hornsea-project-one> Accessed on 1 November 2023). These two projects are adjacent to one another and thus function essentially as a single entity.

In addition to projections for rapid increases in the number of wind turbines being deployed offshore, the distance to the shore is also projected to increase, continuing a trend already manifest in Europe. The distance to the coastline of European offshore wind farms increased by over a factor of four to over 50 km between 2008 and 2019 [5]. However, the majority of offshore wind turbines continue to be bottom-mounted [3] and thus are being deployed in water depths < 80 m [16]. This implies offshore wind farms will be deployed in closer proximity to each other and hence there will be an increasing potential for array–array interactions.

1.3. Wind Turbine Wakes in and from Offshore Wind Farms

The intensity of a wake generated by a wind turbine is determined by the thrust coefficient and hence the wind speed [29]. The downstream recovery of this region of decreased wind speed and increased turbulence (i.e., the wake) [29–31] is primarily dictated by interactions with wakes from other wind turbines [32–34] plus the ambient turbulence and planetary boundary layer depth (PBLH) [14,29,30,35,36]. Turbulence intensities and PBLH are frequently lower offshore than onshore. Further, offshore wind turbine arrays are typically larger [37], employ higher rated capacity wind turbines [38] and more frequently comprise wind turbine layouts that employ a semi-regular or regular grid [39]. These factors combine to mean that wake losses, that are reductions of power generation due to wakes, are considerably larger in offshore wind turbine arrays than onshore.

Average wake losses in onshore wind farms are typically < 5% [40,41], while those from operating offshore wind farms in European waters are larger and increase with decreased wind turbine spacing. For example, Horns Rev I (IC = 160 MW, wind turbine spacing = 7 × 7 rotor diameter (D)) has estimated mean wake losses of 12.4% [32], while Lillgrund (IC = 110 MW, wind turbine spacing = 3.3–4.3 D) has wake losses of 23% [32]. The so-called ‘deep array effect’ has been observed in offshore wind turbine arrays and refers to the low power generation efficiency of wind turbines in the interior of a wind farm due to wake effects [29]. Data from the Nysted offshore wind farm (IC = 166 MW), which has wind turbine spacing of 10.5 D on the west–east axis and 5.8 D in the north–south direction, indicate the interior wind turbines have an average power generation efficiency 15–20% below those on the edge of the wind farm [29,30]. Data from the Anholt wind farm indicate that for freestream turbulence intensity (TI, ratio of standard deviation to wind speed to the mean wind speed (WS)) ~0.06 (6%), a wind turbine located in the center of the array containing one hundred and ten 3.6 MW wind turbines produced, on average, approximately 80% of the power generated by five upstream wind turbines [42]. A scaling analysis using data from two moderately sized offshore wind farms suggested a 1–1.5% increase in total wind farm power generation

efficiency for every 1 D increase in wind turbine spacing (for 4–20 D) and a 1–1.4% increase in total wind farm power generation efficiency for every 1 percentage point increase in TI due to the more rapid erosion of wakes [29]. In this context it is useful to note that while simple engineering models and observational analyses typically report/use TI as a measure of eddy motions in the flow, numerical models such as the Weather Forecasting and Research (WRF) model typically describe the turbulence level using the turbulent kinetic energy (TKE, in m^2s^{-2}). Approximations linking the two metrics include [42]:

$$TI \approx \sqrt{\frac{1.07 \times TKE}{WS}} \quad (1)$$

Naturally, caution should be employed when using such approximations to transform between the two metrics of turbulence and when linking observational and model-derived estimates of turbulence [43]. For example, different model planetary boundary layer (PBL) schemes use different equation closure approaches and thus yield different estimates of TKE [44]. Further, TKE estimates generated by models for finite grid cells are not identical to those reported by pseudo point measurements with sonic anemometers [45].

Conceptually, the kinetic energy that is potentially available for extraction by wind turbines scales with the geostrophic wind speed at the top of the atmospheric boundary layer (ABL). The ABL is the layer of the atmosphere which is coupled to the underlying surface and through which turbulent eddies initiated at the surface extend [46]. Past research has used a range of modeling tools to derive estimates of limits on wind energy extraction that arise from limitations in the vertical renewal rate of kinetic energy from aloft to replace energy extracted by wind turbines operating in very large wind farms. Some have suggested that for wind farms covering areas of 10^4 to 10^5 km^2 the limit on the maximum power production per wind farm area is ~ 1 Wm^{-2} [47]. Others have argued that it may be 3 Wm^{-2} or more, depending on the precise wind turbine spacing [48]. While the current generation of operating wind farms and wind farm clusters lies below the areal extents used to theorize these limits, the largest wind farm lease area cluster considered here is $\sim 3.7 \times 10^3$ km^2 and thus is approaching the size at which substantial reductions in energy extraction efficiency have been postulated.

Until recently, most wind turbine wake research has focused on power losses within individual wind farms (or wind turbine arrays). However, the prevalence of low ambient turbulence intensity, stable stratification and low PBLH offshore favor not only large wake losses within individual wind farms but also large downstream propagation of whole wind farm wakes and potential array–array interactions. [49,50]. Average velocity deficits at 10 km downstream of the UK Westernmost Rough offshore wind farm (210 MW) ranged from 8% and 4% of the freestream wind speed when estimated from ground-based Doppler radar observations and satellite-based synthetic aperture radar, respectively [51]. Case studies of Doppler radar data from Westernmost Rough indicated the wake region extends at least 17 km downstream of this wind farm [52]. The X-Wakes experiment in the German Bight involved use of a scanning Doppler lidar and showed evidence for significant wake interactions between wind farms displaced by 50 km [53]. Analyses of the flight data from a multi-hole flow probe in the same region of the North Sea indicated wind farm wakes were detectable tens of kilometers downwind of the Amrumbank West (302 MW), Nordsee Ost (295 MW) and Meerwind Sud/Ost (288 MW) wind farms under southerly flow and low turbulence intensity [54]. Subsequent analyses of these data combined with an engineering wind farm wake model indicate that for a wind farm cluster comprising approximately 150, 6 MW, wind turbines the average wake length (i.e., the distance at which the wind speed has recovered to 95% of the freestream) was >50 km under stable stratification, while under natural and unstable conditions the wake length was ~ 15 km [55].

Most numerical studies of whole wind farm wakes have employed the Weather Research and Forecasting (WRF) model [56]. WRF is a state-of-the-art regional numerical weather prediction model based on Reynolds-averaged Navier–Stokes equations of the atmosphere. It is widely applied within the wind energy community and has also been used

to make wind resource assessment and power production projections [57,58], wind resource assessment in an evolving climate [59,60] and for short-term forecasting [61–63]. Multiple wind farm parameterizations (WFPs) have been developed for use with WRF [43,56]. By far the most commonly used are Fitch [64] and the explicit wake parameterization (EWP) [65]. These WFPs are designed to compute the power production from wind turbines within wind farms and represent the production, advection and dissipation of wind farm wakes. They use information about the physical dimensions (hub height and rotor diameter) plus the power curve to quantify electrical power production. The wind turbine thrust coefficient, which also varies with hub-height wind speed, is used to represent the drag imposed in each model grid cell across the rotor plane and modify the wind profile accordingly. In EWP, the velocity deficit (wake) generated by each wind turbine is assumed to have a Gaussian form that decays with vertical distance from the hub-height following an exponential form and of a magnitude that scales with the thrust coefficient. In the Fitch parameterization, momentum is only extracted from model levels that intersect the rotor plane. The wake-induced velocity deficit within the wind speed profile enhances the shear-induced turbulent kinetic energy (TKE). In Fitch, the wind turbine rotor additionally acts as an active TKE source in an amount proportional to the fraction of kinetic energy extracted by the wind turbine that is not converted into electrical power. The amount of TKE added to the flow due to the rotor action in the current WRF–Fitch WFP (WRF v4.2.2) the default has been reduced to 0.25 of the original value specified by Fitch based on output from large eddy simulations (LESs) [66]. In EWP, wake expansion due to the increase in grid-cell average TKE is treated using a sub-grid turbulence diffusion equation. Accordingly, both within wind farm and between wind farm wakes from two WFPs (Fitch and EWP) exhibit important differences, particularly under low ambient TKE [34,43,67,68]. Model evaluations, that have largely been confined to case studies due to data limitations, have found divergent results in terms of which WFP best represents wakes within and downwind from offshore wind farms [43,52,69–72].

Downstream advection of TKE generated by the action of wind turbine rotors in the Fitch scheme has not been appropriately treated in all WRF releases. It was appropriately advected within the MYNN planetary boundary layer (PBL) scheme in WRF versions 3.3 and 3.4 and in v3.5 if the namelist flag ‘myynn_tkeadvect’ is set to true. It is not properly treated in releases starting with v3.6 (see details at <https://github.com/wrf-model/WRF/releases?after=v4.0.1> Accessed on 1 November 2023). The coding error is not present in WRF v4.2.2 which is the version used herein, and a patch to correct the error was applied to WRF v3.8.1 prior to compiling the model that was used in our previous simulations with WRF v3.8.1 [14]. However, it is likely that this error was present in a number of published studies, though as has been previously noted [56], the lack of fully traceable information about the simulation configuration makes identifying the presence of such errors very challenging.

1.4. Objectives

The objectives of research reported herein are as follows:

- To quantify likely power production from offshore wind energy lease areas along the U.S. east coast and how power production efficiency varies across a range of plausible installed capacity densities (ICDs) and between two widely used wind farm parameterizations.
- To quantify whole wind farm wake extents and power losses due to both internal and external wakes and how they scale with ICD. We further quantify the likely effect from wakes generated by the ‘second-generation’ of lease areas along the U.S. east coast on the ‘first-generation’ lease areas in which wind farms are currently being developed.
- To examine the dependence of projected power output from the largest wind energy cluster (3675 km²) on ICD (3.5 to 6 MWkm^{−2}) in the context of previous research on wind power density limits.

2. Materials and Methods

2.1. Simulations

Simulations were performed using the WRF model (v4.2.2) with the Fitch and EWP wind farm parameterizations active (Table 1). The outermost domain, d01, uses a grid spacing (dx) of 16.67 km, while d02 uses dx = 5.56 km (Figure 1). The three innermost domains (d03, d04 and d05) use dx = 1.85 km and a time step of 5.3 s. These domains are used to simulate freestream conditions without wind turbines (d03), wind turbine power generation and wakes computed using Fitch (d04) and wind turbine power and wakes computed using EWP (d05). There are 57 vertical levels, 20 of which are below 370 m. Wind speeds from the ninth level (mean height for offshore grid cells ~143 m) are used here to represent flow at the wind turbine hub height. The MYNN2.5 PBL scheme is used because the Fitch WFP was designed for use with this scheme, although Fitch has recently been coupled to an alternative PBL scheme [73].

All of the wind energy offshore lease areas (LAs, referred to as OCS-A NNNN, [74]) considered here are in the high wind resource areas [12] along the coasts of the northeast and Atlantic U.S. states (Figure 1). Fifteen of these lease areas that were auctioned prior to 2020 are considered here (listed by original LA number) and are grouped into LA clusters in recognition that although they may have different owners and even unique configurations they are in sufficiently close proximity and have sufficient individual areal extent that power production is mutually dependent [75]:

- LA1–7 (OCS-A 0486, 0487, 0500, 0501, 0520, 0521, 0522) collectively cover 3675 km² and are south of Massachusetts (MA) and Rhode Island (RI).
- LA8 (OCS-A 0512) is located off the coast of New York (NY), south of Long Island, and covers 321 km².
- LA9–13 cover a total area of 2105 km² and lie east of New Jersey (NJ) (OCS-A 0499 and 0498), Delaware (DE) (OCS-A 0482 and 0519) and Maryland (MD) (OCS-A 0490).
- LA14 and 15 (OCS-A 0483 and 0497) cover an area of 465 km² and are located east of Virginia (VA).

These lease areas are under various stages of development and were subject to earlier WRF simulations with the Fitch wind farm parameterization active [14]. The results of that study indicated that deployment of a 15 MW wind turbine with a spacing of 1 nm (1.85 km) in these lease areas would generate 116 TWh of electricity per year, or approximately 3% of current U.S. demand.

Table 1. Overview of the simulation settings.

Layout	d01	d02	d03/04/05
Grid spacing (dx in km)	16.67	5.56	1.85/1.85/1.85
Wind farm parameterization	-	-	-/Fitch/EWP
Longwave radiation	Rapid radiative transfer model (RRTM) [76]		
Shortwave radiation	Dudhia [77]		
Microphysics scheme	Eta [78]		
Cumulus scheme	Kain–Fritsch [79]		-/-/-
Surface layer	MM5 similarity [80]		
Land surface model	Noah [81]		
PBL scheme	Mellor–Yamada–Nakanishi–Niino 2.5 (MYNN2.5) [82]		

The LA clusters described above are referred to herein as the ‘first-generation’ of LA clusters (Figure 1b). One of the four new sets of WRF simulations presented here also considers lease areas that were auctioned in February 2022. This ‘second-generation’ LA cluster comprises those located in the New York Bight which is the coastal area between Long Island and the New Jersey coast. All of these new lease areas also have unique

identifiers (listed from north to south); OCS-A 0544, 0537, 0538, 0539, 0542 and 0541. They cover an area of 1970 km² and are collectively referred to herein as NYBig (Figure 1a,b). Where results are synthesized into LA clusters these new lease areas are grouped with LA8 and referred to as NYBIG.

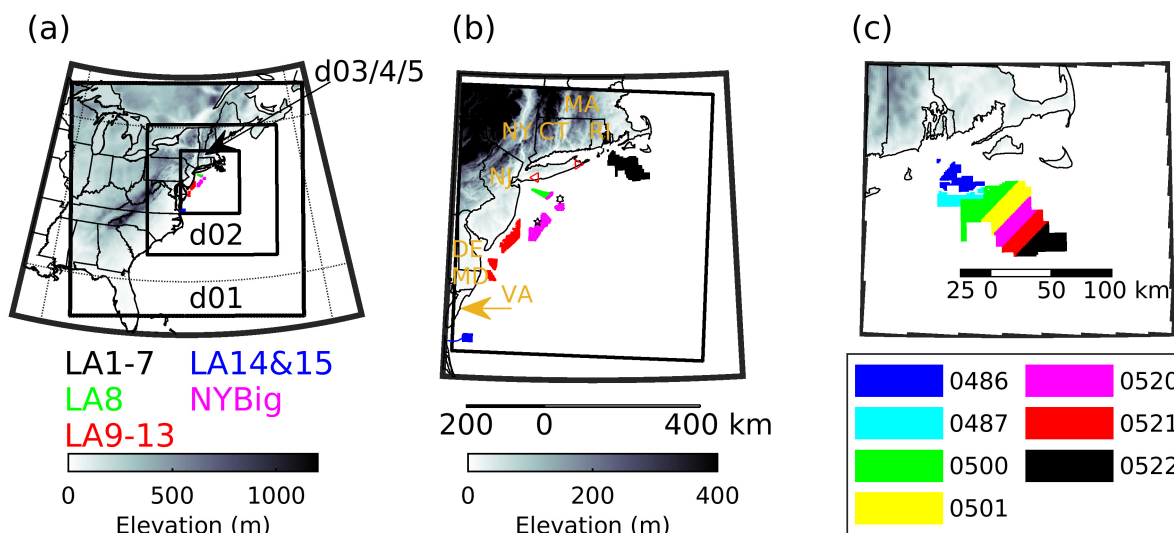


Figure 1. (a) WRF simulation domains, topography and the location of the wind turbine lease areas considered (colored areas). (b) Innermost simulation domains (d03, d04, d05) with the lease area clusters identified. The area covered by these domains is denoted by the black outline box in which the terrain elevation is shown. The states are labeled with a two-letter designation: NY = New York, MA = Massachusetts, CT = Connecticut, RI = Rhode Island, DE = Delaware, MD = Maryland and VA = Virginia. The black hexagon and pentagon denote the locations of buoys E05 and E06 on which lidars have been deployed. The red triangles show the locations of two NYMesoNet sites that have lidars deployed and are closest to the coast; EHAM and WANT [83]. (c) Detail of the LA cluster south of Massachusetts and Rhode Island with the individual lease areas as originally auctioned shown by the four digits of the unique identifier.

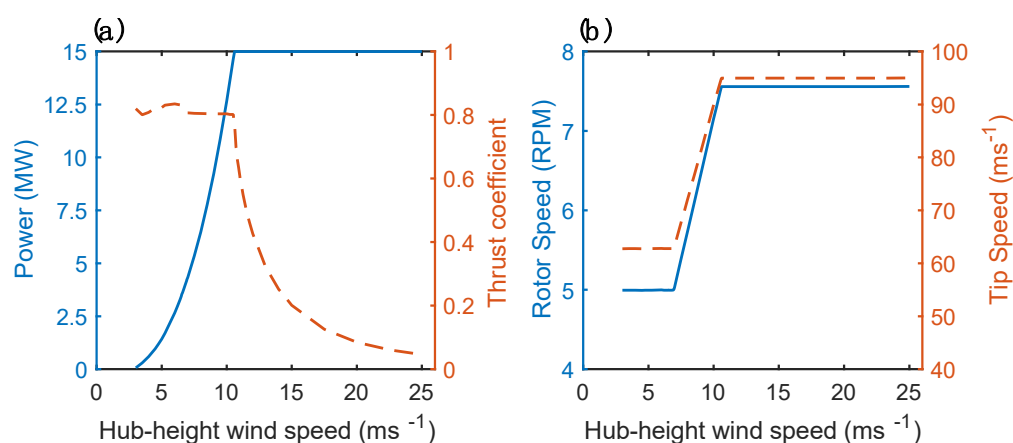
In total, 44 simulations comprising 231 days were performed. This ensemble contains simulations for four wind turbine layouts that reflect different wind turbine deployment strategies. The four different wind turbine layouts (Table 2) are as follows:

- CNTRL: Wind turbines are deployed on a regular grid separated by 1.85 km in LA1–15. For the 15 MW wind turbine considered herein this spacing results in a mean ICD $\sim 4.3 \text{ MWkm}^{-2}$, and it equates to a separation distance of $\sim 7.7 D$ which is approximately the mean value for operating offshore wind farms in Europe [27].
- CORRI: Wind turbines are deployed on a regular grid separated by 1.85 km in LA1–15 (as in CNTRL) but every sixth north–south row is removed to generate marine corridors. The resulting mean ICD is $\sim 3.5 \text{ MWkm}^{-2}$. Based on publicly available data, the world’s largest offshore wind project, Hornsea 1 and 2, have a similar average ICD of $\sim 3 \text{ MWkm}^{-2}$.
- 6MWSQ: Wind turbines are deployed at a higher density in LA1–15 for a mean ICD $\sim 6 \text{ MWkm}^{-2}$ and an average separation distance of $\sim 1.6 \text{ km}$ ($\sim 6.7 D$). This ICD is similar to that of the Rødsand offshore wind farm in Denmark that covers 35 km². It is also an ICD scenario considered in the Agora study of possible offshore wind energy expansion in the German Bight [84].
- NYBIG: Wind turbines are deployed as in the CNTRL layout for all of the ‘first-generation’ LAs plus those auctioned in the New York Bight (NYBig) in February 2022. As in CNTRL the mean ICD is $\sim 4.3 \text{ MWkm}^{-2}$.

Table 2. Overview of the wind turbine layouts.

Layout	CNTRL	CORRI	6MWSQ	NYBIG
ICD (MWkm^{-2})	4.3	3.5	6.0	4.3
Total areal coverage of wind turbines (km^2)	6566	6566	6566	8536
Total number of 15 MW wind turbines	1922	1604	2598	2495
Installed capacity (MW) by LA cluster				
LA1–7	16,095	13,500	22,275	16,095
LA8 (plus NYBig for NYBIG)	1335	1110	1875	9930
LA9–13	9360	7815	12,195	9360
LA14 and 15	2040	1635	2625	2040

Power and thrust curves are not widely available for commercial wind turbines. Hence, the International Energy Agency (IEA) has developed a 15 MW reference wind turbine that can be used in studies such as that presented herein (Figure 2). This wind turbine is an International Electrotechnical Commission (IEC) Class 1B and has a hub height of 150 m and a rotor diameter of 240 m [85]. It is designed to represent the overall dimensions, rated power and performance of wind turbines being deployed offshore.

**Figure 2.** (a) Power and thrust coefficients plus (b) rotor speed and tip speed as a function of hub-height wind speed for the IEA 15 MW reference wind turbine [85].

The ERA5 reanalysis [86] was used to derive representative flow conditions and select the periods used to perform the simulations presented herein and to provide the lateral boundary conditions for the WRF simulations. The methodology by which the simulation periods are selected has been described previously [14] but in brief is as follows: Forty years of hourly ERA5 wind speed and direction at 100 m AGL at the center of the NY lease area (LA8, Figure 1) were used to quantify the frequency of flow in four wind direction sectors (SW: 180–270°, NW: 270–360°, NE: 0–90°, and SE: 90–180°) and four wind speed classes that differ in terms of their likely wake generation via the thrust coefficient: 0–4 ms⁻¹ (no wakes because the wind turbines are not generating electricity and thus are not extracting momentum, Figure 2a), 4–10 ms⁻¹ (wakes as the wind turbines are generating electricity and extracting momentum at relatively high thrust coefficient values), 10–16 ms⁻¹, 16–25 ms⁻¹ (the wind turbines are operating at rated power) and >25 ms⁻¹. Three-quarters of all hours can be classified into one of ten combinations of wind direction and wind speed. The same ERA5 time series was scanned to identify five-day periods with the maximum number of hours that conform to each flow scenario (Table 3) and that occur in the season where that flow scenario is most frequent. For the most frequent flow scenario (NW4–10), two cases, one in late autumn and one in summer, are simulated.

Table 3. Definitions of the flow scenarios, their frequency and the five-day simulation periods used to represent them. The flow cases are listed in chronological order of the five-day simulation period. Two cases are used to represent northwesterly flow in the wind speed class 4–10 ms^{−1} at 100 m, one in the autumn (26 October 1979, i.e., 1979-10-26) and one in early summer (1998-06-04), thus the frequency of this class, 15.7%, is applied as 7.85% to the first case and 7.85% to the second. The final columns show the areal extent (expressed as the percent of the innermost simulation domain after removing the outer 10 grid cells along each edge of the domain) of a mean velocity deficit of ≥5% (i.e., $\langle v_d \rangle \leq -0.05$) for each of the 5-day simulation periods (flow scenarios) and the four layouts computed using output from the Fitch and EWP wind farm parameterizations.

		Layout	CNTRL		CORRI		6MWSQ		NYBIG	
		ICD (MWkm ^{−2})	4.3		3.5		6.0		4.3	
		Areal Coverage of Wind Turbines (km ²)	6566		6566		6566		8536	
Flow Scenario (WDWS)	Percent Frequency	Five-Day Simulation Period (YYYY-MM-DD)	Fitch	EWP	Fitch	EWP	Fitch	EWP	Fitch	EWP
NW4–10	7.85	1979-10-26 to 1979-10-30	2.49	1.95	2.24	1.62	2.79	2.40	3.21	2.48
SW16–25	1.6	1981-04-04 to 1981-04-08	4.02	2.23	3.54	1.74	4.73	3.04	5.53	3.09
SE4–10	7.5	1981-08-29 to 1981-09-02	5.50	4.50	5.03	4.09	5.80	5.07	7.19	5.96
NE10–16	4.6	1985-11-28 to 1985-12-02	3.81	2.51	3.25	1.97	4.71	3.35	5.56	3.70
SW10–16	9.1	1986-03-26 to 1986-03-30	7.02	4.94	6.44	4.15	8.00	6.13	9.59	7.15
SW4–10	12.5	1988-07-04 to 1988-07-08	7.51	6.44	6.71	5.50	7.67	7.97	10.36	8.61
NW4–10	7.85	1998-06-04 to 1998-06-08	3.41	2.70	3.13	2.35	3.71	3.14	4.72	3.78
NW16–25	1.4	2000-01-17 to 2000-01-21	1.79	0.79	1.41	0.46	2.33	1.51	2.11	0.80
NW10–16	11	2007-02-05 to 2007-02-09	1.75	0.80	1.40	0.48	2.20	1.45	2.15	0.88
SE10–16	2.3	2011-05-15 to 2011-05-19	4.22	2.51	4.55	2.49	5.68	3.92	6.28	3.70
NE4–10	9.6	2012-11-17 to 2012-11-21	4.32	3.16	3.66	2.53	5.34	4.40	5.95	4.60

The flow scenarios are referred to herein using WDWS: YYYY-MM-DD where WDWS refers to the dominant wind direction and wind speed class (e.g., SW4–10 indicates predominantly southwesterly flow with wind speeds between 4 and 10 ms^{−1}) (Table 3). The digits after the colon denote the calendar date corresponding to the first day of the five-day period (e.g., 1998-06-04 indicates the 4 June 1998). As in our previous research [14], simulations are performed for each layout using 11, 5.25-day, periods that represent frequently occurring flow scenarios. The results are frequency weighted by the flow case to generate a representative climatology. For each simulation the first 6 h is used as a model spin-up period and results are presented for the subsequent 120 h, with output at a 10 min disjunct frequency.

2.2. Data Analyses

In all results presented herein a 10-grid-cell buffer zone along the west, south, east and north of the d03/d04/d05 domain is excluded to avoid edge effects of flow adjustment across domains with different resolutions. Output for a 6 h spin-up period is also excluded, leaving 5 days of output at a 10 min time interval for use in the analyses.

A range of metrics are used here to describe the projected power production, capacity factors and wake intensity and extent from the WRF simulation ensemble (Table 4). Power production estimates reported here derive directly from the WFP and are determined by the power curve and modeled wind speed (Figure 2). Capacity factors (CFs) reported here describe the ratio of the power produced according to each WFP divided by the total power that could have been produced if all wind turbines were operating at the rated power of 15 MW. Wake-induced power losses are computed by applying the freestream wind speeds at each grid cell containing a wind turbine(s) to the power curve and computing the

electrical power that would be created if each wind turbine was acting as an isolated (i.e., unyawed) wind turbine.

Table 4. Précis of metrics used to describe power production and wind turbine wake intensity and areal extent.

Metric	Description	Calculation Method (and Equation #)
Power production (<i>PP</i> in MWh)	Annual electrical power production in MWh from wind turbines	$PP = \sum_{j=1}^{11} F_j \times \frac{1}{6} \times \sum_{i=1}^{720} \sum_{n=1}^m Power(f(WS))_n \times \frac{8760}{11 \times 120} \times \frac{1}{10^6} \quad (2)$ <p>$\sum_{i=1}^{720} \sum_{n=1}^m Power(f(WS))_n$ = sum of power (in W) in each grid cell with wind turbine(s) ($n = 1$ to m) output every ten minutes ($i = 1$ to 720) from the WRF-WFP and computed via the power curve (division by 6 is to convert to Wh). $\sum_{j=1}^{11} F_j$ = frequency weight of each of the 11 cases ($j = 1$ to 11) and then the resulting power is summed. The last two terms are first to scale to the number of hours in a full year from the number of simulated hours, and then to convert to MWh from Wh</p>
Capacity factor (<i>CF</i> in %)	Simulated power production (<i>PP</i>) divided by that possible if all wind turbines operated at their rated capacity in each hour of the year	$CF = \frac{PP}{Total\ installed\ capacity \times 8760} \quad (3)$
Wake-induced power losses (<i>WL</i> in MWh)	Amount of power production suppression due to wake reduction of inflow wind speed	$WL = PP - PosP$ $PosP = \sum_{j=1}^{11} F_j \times \frac{1}{6} \times \sum_{i=1}^{720} \sum_{n=1}^m Power(f(WS_{freestream}))_n \times \frac{8760}{120 \times 11} \times \frac{1}{10^6} \quad (4)$ <p>Potential power from each wind turbine computed from freestream windspeed (output from domain d03, $WS_{freestream}$) minus calculated power production from WFP</p>
Wake-induced velocity deficit	Normalized difference between wind speed computed at a given location and time from d04 or d05, relative to the freestream (domain d03)	$v_d = \frac{WS_{WT(x,y,i)} - WS_{NoWT(x,y,i)}}{WS_{NoWT(x,y,i)}} \quad (5)$ <p>$WS_{WT(x,y,i)}$ indicates the wind speed when the WFP is operational (i.e., output from domain d04 (Fitch) or d05 (EWP)), WS_{NoWT} denotes WS from the same location (x,y) and time stamp (i) but for domain 03</p>
Normalized wake extent (<i>NWE</i>)	Area with a velocity deficit of a given magnitude (X) divided by the footprint of the wind farm/lease area cluster	$NWE = \frac{Area_{v_d \leq X}}{Area_{LAcluster}} \quad (6)$

There are two possible mechanisms via which simulations with the two wind farm parameterizations (Fitch or EWP) can yield differences in CF or wake-induced power losses from a given wind farm, lease area cluster or the entire system of wind turbines. First, the WFPs can differ in terms of the rapidity with which the wind farm wakes are eroded as they move downwind and hence the probability that an upstream cluster of lease areas will reduce the inflow wind speed to downwind clusters. Secondly, the WFPs can yield differences in the wakes internal to the wind farm lease areas, and thus the degree to which these WFP reproduce the ‘deep array effect’. We quantify the spatial extent of whole wind farm wakes (see details below) and further compare CF from the ‘first-generation’ of LA clusters with and without the addition of the ‘second-generation’ of lease areas in the NY Bight to quantify the impact that these lease areas may have on the power production efficiency in the other lease areas. To illustrate the degree to which the simulations manifest a deep array effect, we perform targeted analyses of simulation output from the LA cluster 1–7 (south of Massachusetts and Rhode Island). For each flow case we select 50 grid cells with the lowest power production to represent the most severely waked wind turbines and 50 grid cells with the highest power production to represent the power at the edge of the cluster where the wind turbines are least likely to experience wake effects. We compute for each layout and flow scenario the ratio of the mean power produced for those two samples and the mean probability that any one of those interior or exterior grid cells in any 10 min period will experience zero power production. This analysis is consistent with the manner in which observational data have previously been analyzed [30], but due to wind directional variability, the 50 exterior grid cells may not consistently experience fully undisturbed (‘freestream’) conditions.

Wake intensity and spatial extent are characterized using the velocity deficit (v_d) at the wind turbine hub height in each grid cell at each simulation time step (Table 4). Two summary metrics are derived for v_d in a given grid cell. (i) The mean v_d ($\langle v_d \rangle$) for a given flow scenario (i.e., the mean v_d computed from 720, 10 min, data output intervals). (ii) The marginal probability of $v_d \leq -0.05$ for a randomly drawn model time

step ($\Pr(v_d \leq -0.05)$). A two-sample *t*-test with a threshold *p*-value of 0.01 is applied to assign statistical significance to $\langle v_d \rangle$ based on the mean pairwise differences in wind speed (d04 or d05 from d03). As in our previous research [14], these test results are corrected for multiplicity [87].

The spatial extent of wakes is presented in two forms, the fraction of the inner-most simulation domain that is covered by wakes of a given intensity (in Table 3 this wake extent is for a $v_d \leq -0.05$) and in terms of the normalized wake extent (NWE, Table 4). The NWE describes the areal extent of a wake of a given intensity (e.g., $v_d \leq -0.05$) divided by the areal extent (or footprint) of the LA clusters.

As shown herein, the northernmost LA cluster is seldom influenced by remotely generated wakes that have a $\geq 5\%$ velocity deficit relative to the freestream (i.e., $v_d \leq -0.05$). Thus, to illustrate the physical dependencies of NWE and to develop a simple emulator of NWE, an analysis is performed using data from only this cluster (LA1–7). An emulator is a term applied to simple models that replicate (or emulate) the behavior of more complex model systems. In this case the emulator is built using stepwise multiple linear regression with an intercept term and linear and squared terms for each predictor, plus first-order interactions. Terms are included (or excluded) based on a change in *p*-value (threshold of 0.05) for an F-test applied to the sum of squared error resulting from addition or removal of the term [87]. Three primary parameters are used as predictors of NWE: (i) Wind speed, (ii) TKE and (iii) PBLH in the center of the LA1–7 cluster from the d03 (freestream) output for ICD of 4.3 MWkm^{-2} . To enhance the stability of this emulator, the predictors are sub-set into 125 classes prior to construction of the model. The classes are defined by dividing values of each parameter into five percentile-based classes: 0–20th percentile, 20–40th percentile, etc., and then combining samples in each joint occurrence to compute a mean freestream WS, TKE and PBLH and the associated mean NWE. As an example, all 10 min periods with a WS in the 40th to 60th percentile interval and TKE in the 20–40th percentile interval and PBLH in the 60–80th percentile interval are used to compute the mean NWE from Fitch and EWP which serves as the predictand and a mean value of each of the three predictors. The emulators are then applied to the raw 10 min time series of predictors to evaluate the model skill relative to the high-frequency NWE derived from Fitch and EWP.

Analyses of the WRF simulation output also include evaluation of the freestream wind climate from domain d03 relative to data from vertically pointing lidars deployed on buoys by the New York (NY) State Energy Research and Development Authority (NYSERDA) and within the New York State Mesonet [83]. The buoys on which the lidars were mounted were deployed in OCS-A 0537 (Hudson North E05) and OCS-A 0539 (Hudson South E06) (Figure 1) [88]. There are multiple periods with missing data due to instrument failure and the measurement records are relatively short: August 2019 to September 2021 for E05 and September 2019 to February 2022 for the E06 buoy, which may negatively impact the degree to which the resulting data reflect the true wind climates. The two sites from the NY Mesonet are both on Long Island and are the two lidar sites closest to the coast and the offshore wind energy lease areas. They are EHAM in east Hampton and WANT at Wantagh. Based on measurements from January 2019 to December 2022, data recovery for wind speeds at 150 m is 65–70% and there is a bias towards over-representation of summer months [83]. Thus, a climatological record is reconstructed by assuming the missing data are not biased towards particular wind speeds and resampling wind speed measurements from under-sampled months. These observations provide an opportunity to examine the degree to which the simulation periods exhibit a similar wind climate in terms of hub-height wind speed and wind direction to those sampled by the lidars. Additional evaluation of the degree to which the climatology generated from the periods simulated herein is representative is performed using hourly output from an earlier long-term WRF simulation [89]. This NOW-23 modeled data set was produced using WRF (v4.2.1) nested within ERA5 for January 2000 to December 2020. The simulations used the MYNN PBL scheme and two nests with $dx = 2 \text{ km}$ in the inner domain. This inner domain covers

the upper two-thirds of the innermost domains considered herein and thus has output available for LA1–7, LA8 and LA9–13.

3. Results

3.1. Power Production, Capacity Factors and Efficiency

Total U.S. electricity consumption in 2021 was 3930 TWh (U.S. Energy Information Administration (EIA); <https://www.eia.gov/energyexplained/electricity/use-of-electricity.php>, access date of 1 November 2023). Currently, land-based wind turbines supply approximately 10% of this total U.S. electricity consumption (<https://www.eia.gov/energyexplained/wind/electricity-generation-from-wind.php>, access date of 1 November 2023). This can be compared with projected total annual power generation from the U.S. east coast LAs. Frequency-weighted power production for the CNTRL, CORRI, 6MWSQ and NYBIG layouts are 108, 95, 132 and 139 TWh/yr, respectively, based on output from Fitch and 134, 116, 170 and 173 TWh/yr based on output from EWP. Thus, if all of the lease areas considered herein were subject to deployment of 15 MW wind turbines with a spacing of 1.85 km (i.e., NYBIG), they are projected to supply between 3.5% (Fitch) and 4.4% (EWP) of total national annual electricity consumption.

All four wind turbine layouts yield relatively high climatologically representative (i.e., frequency-weighted) mean capacity factors (CFs) for the entire system and each LA cluster (Table 5 and Figure 3). CF variations between the LA clusters are largely a function of two factors. LA clusters with the lowest CF are due to either lower wind resources in the southern lease areas (LA14 and 15, Figure 3 inset) or larger wake losses in the largest LA cluster (LA1–7).

Table 5. Frequency-weighted mean CF (in %) from EWP and Fitch for all lease areas (All LAs) and each LA cluster and wind turbine layout. Final rows show fractional normalized difference in the frequency-weighted CF for each LA cluster and layout: (Fitch-EWP)/Fitch. * Note: LA8 = LA8 + NYBig for NYBIG.

WFP: Lease Areas	System-Wide, i.e., All LAs	LA1–7	LA8 *	LA9–13	LA14 and 15
EWP: CNTRL	53.2	53.1	61.2	53.3	47.6
EWP: CORRI	54.9	54.9	62.4	55.0	48.5
EWP: 6MWSQ	49.7	49.2	58.3	50.0	45.2
EWP: NYBIG	52.6	53.0	52.7	51.5	47.6
Fitch: CNTRL	42.9	42.6	51.6	42.7	39.5
Fitch: CORRI	44.8	44.7	53.0	44.7	40.6
Fitch: 6MWSQ	38.7	38.1	47.7	38.9	36.4
Fitch: NYBIG	42.4	42.6	42.6	41.2	39.6
Normalized difference: (Fitch-EWP)/Fitch					
CNTRL	−0.24	−0.25	−0.19	−0.25	−0.20
CORRI	−0.23	−0.23	−0.18	−0.23	−0.20
6MWSQ	−0.28	−0.29	−0.22	−0.29	−0.24
NYBIG	−0.24	−0.24	−0.24	−0.25	−0.20

Discrepancies between mean CFs projected using simulations with the two WFPs are most pronounced for the highest wind turbine densities and for the largest LA clusters (Table 5 and Figure 3), reflecting important differences in predicted wake losses from the two WFPs. The system-wide CFs computed from EWP of 50–53% for ICD of 6 MWkm^{−2} and 4.3 MWkm^{−2} distributed over 6566 km² compare favorably with estimates from the Agora analysis of the North Sea German Bight that also used the EWP

and WFP and indicated that for a developed area of 2767 km² at an ICD of 6 MWkm⁻² the CF was 42% [84].

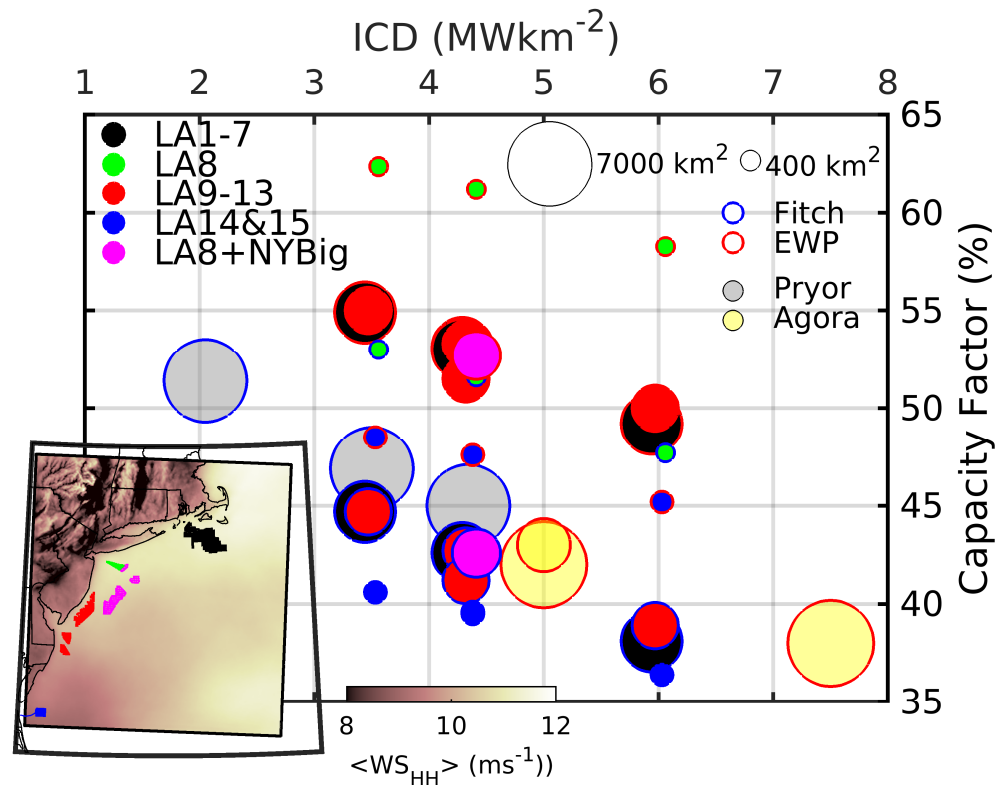


Figure 3. Frequency-weight mean CF for each LA cluster for CORRI (ICD ~ 3.5 MW km⁻²), CNTRL (ICD ~ 4.3 MW km⁻²) and 6MWSQ (ICD ~ 6 MW km⁻²), plus the NYBIG (ICD ~ 4.3 MWkm⁻² in the original 15 LA and NYBig). Marker fill colors denote the LA cluster (upper left legend), the size of the dot denotes the area over which wind turbines are deployed in each LA cluster and the outer marker edge color denotes the wind farm parameterization used (upper right legend). Also shown are (1) results from the Agora study which used WRF with EWP and considered large deployments in the German Bight of the North Sea (Agora); (2) mean CF for all of the 15 original LAs for three different layouts; CNTRL, CORRI and a half density (ICD approx. 2.1 MWkm⁻²) from the earlier simulations with WRF v3.8.1 and the Fitch wind farm parameterization (Pryor) [14]. The map in the lower left shows the locations of the LA clusters and the background is the mean freestream wind speed at approximately hub height.

Output from the NYBIG layout (i.e., including the ‘second-generation’ LA in the New York Bight) versus the CNTRL indicates that deployment of wind turbines in that ‘second-generation’ of LA appreciably reduces inflow wind speeds over LA8 and LA9–13. It decreases CF in the original LA8 by approx. 8 percentage points based on both Fitch and EWP (Table 5). Comparison of climatologically representative CFs from the CNTRL and NYBIG simulations also implies that advection of the whole wind turbine array wakes from NYBig will reduce CF in LA9–13 by approx. 1.5 percentage points. Little or no effect is found on CF from LA1–7 or LA14 and 15 due to the presence of wind turbines in these ‘second-generation’ LAs (Table 5).

As expected, the power production efficiency as measured using the CF from the largest wind farm cluster (LA1–7, areal extent 3675 km²) substantially declines as the ICD increases (3.5, 4.3 to 6.0 MWkm⁻²) in simulations with both Fitch and EWP (Table 5). However, the power production per wind farm area increases over this ICD increases from ~ 1.64 , to 1.87 and then to 2.31 Wm⁻² in output from Fitch as ICD increases from 3.5 to 4.3 and then to 6.0 MWkm⁻². Power production per wind farm area increases from ~ 2.02 to 2.33 to 2.98 Wm⁻² in output from EWP over this range of ICD. Thus, all values

are substantially above the lower estimate for maximum power production per unit area of $\sim 1 \text{ Wm}^{-2}$ derived for wind farms covering areas of 10^4 to 10^5 km^2 . The implication is that although this cluster of lease areas is unprecedented in terms of currently operating offshore wind farm clusters, for the range of ICD considered here, it does not appear to approach the extent at which substantial efficiency reductions have been theorized to occur due to limits on kinetic energy recharge.

Wake-induced power production losses are computed as the difference between the power generation from the two WFPs and the power generation estimate assuming the wind turbines all experienced the freestream wind speed from d03 normalized by the system-wide power production computed by assuming all wind turbines experience the freestream wind speed (see Table 4). Consistent with expectations, these climatological wake losses (derived by frequency weighting values from each of the 11 flow cases) are highest for the 6MWSQ layout and smallest for the CORRI layout. They are 27–37% (Fitch) and 11–19% (EWP). Wake losses for NYBIG slightly exceed those from CNTRL in both WFPs. For example, the climatological mean wake loss in the CNTRL layout computed from Fitch is 30.2% and for NYBIG it is 31.0%. Nevertheless, system-wide wake losses are substantial for all four layouts. Accordingly, in the following sections we quantify wake characteristics in more detail.

3.2. Wake Extents

The spatial patterns of wake extents (i.e., areas with $\langle v_d \rangle < -0.05$) from Fitch and EWP exhibit a similar dependence on the flow conditions (i.e., across the 5-day simulation periods) and WT layouts (Figure 4). Consistent with expectations, periods with lower wind speeds exhibit larger horizontal wake extents due to the higher wind turbine thrust coefficient (Figure 2). For example, the area covered by $\langle v_d \rangle < -0.05$ for the SW4–10: 1988-07-04 flow case is 7–8% of the innermost simulation domain for the CNTRL layout, while simulations of the NW16–25: 2000-01-17 flow case indicate an areal extent of $\langle v_d \rangle < -0.05$ of 1.5–2.5% of the innermost domain (Figure 4 and Table 3).

The cumulative wake extent increases with the total number of wind turbines installed and is systematically highest for the NYBIG layout and the 6MWSQ layouts (Figure 4 and Table 3). The areal extent of wind farm wakes is also systematically larger for all layouts and all simulation periods in output from the Fitch wind farm parameterization than when EWP is employed (Figure 4). When a composite is made of grid cells with $\langle v_d \rangle \leq -0.05$ for one or more of the flow scenarios (Table 6 and Figure 5) the mean wind shadow is considerably larger when the Fitch WFP is employed irrespective of the ICD and/or the addition of the ‘second-generation’ lease areas (NYBIG). The ratios of the wake extent (Fitch/EWP) across the 11 simulations are 1.18 to 1.38. For the CNTRL layout 12.6% of the innermost simulation domain is covered by a wind farm shadow for one or more of the flow scenarios in output from Fitch, while simulations with EWP indicate a wind shadow that is nearly one-third smaller (Table 6).

Table 6. Percentage of the innermost domain covered by a mean velocity deficit of $\geq 5\%$ ($\langle v_d \rangle \leq -0.05$) for at least one of the flow scenarios (i.e., at least one of the eleven 5-day simulations) for each of the four layouts using output from the EWP and Fitch WFPs.

Layout	Fitch	EWP
CNTRL	12.6	9.84
CORRI	11.5	8.33
6MWSQ	14.2	12.0
NYBIG	16.0	13.3

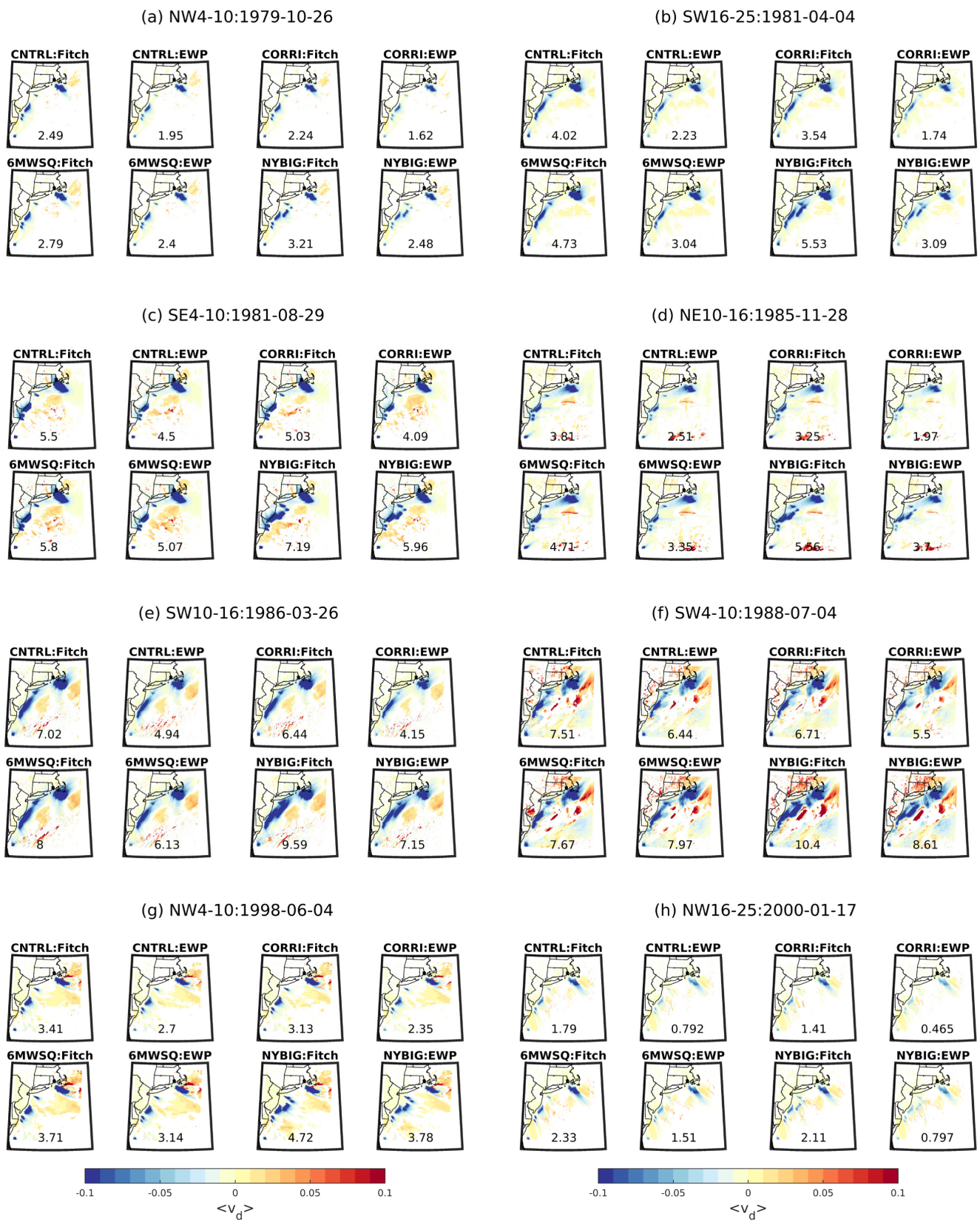


Figure 4. Cont.

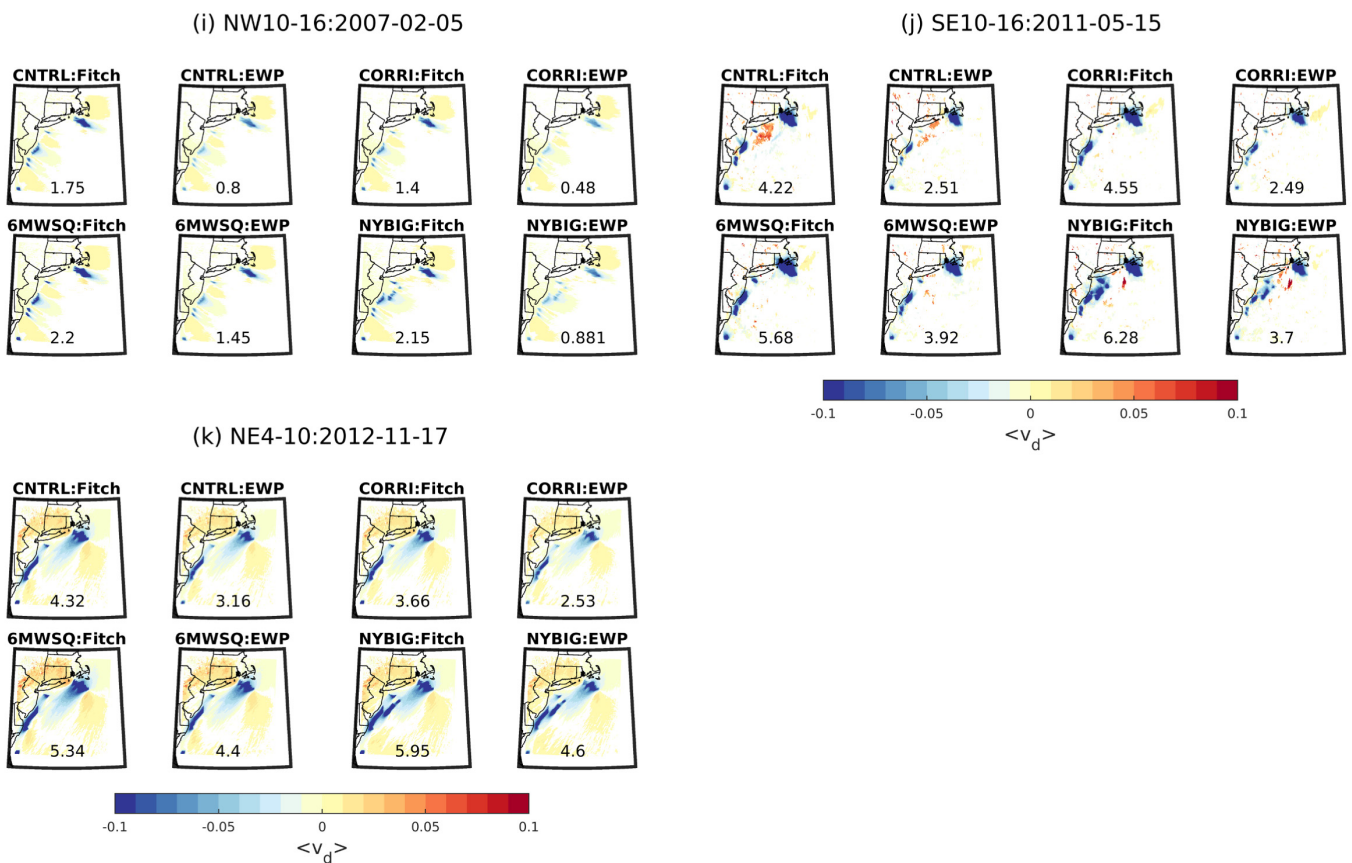


Figure 4. Mean velocity deficit ($\langle v_d \rangle$) computed for each of the 11 flow conditions (panels (a–k)) and the four different wind turbine layouts (sub-panels within each panel) computed using output from Fitch and EWP. The values shown at the bottom of each panel indicate the percentage of the inner-most domain that is covered by $\langle v_d \rangle \leq -0.05$.

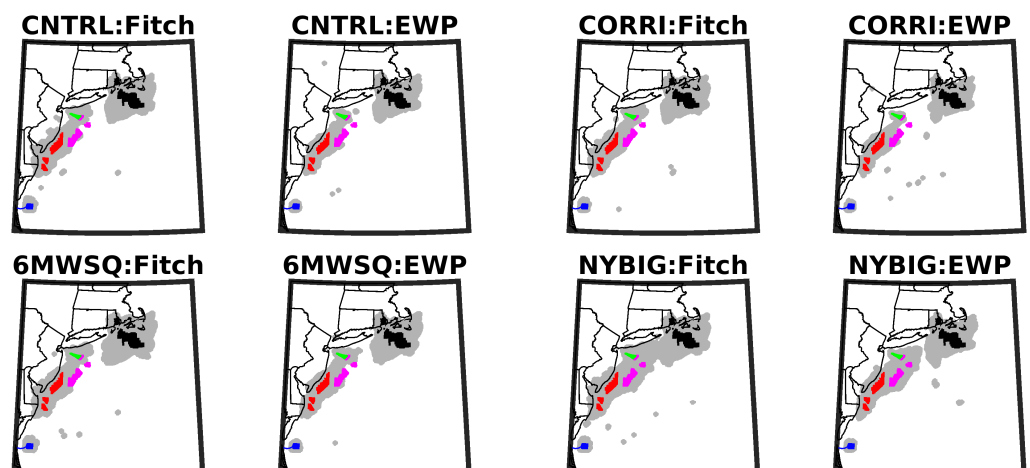


Figure 5. Areas covered by a mean velocity deficit of $\geq 5\%$ ($\langle v_d \rangle \leq -0.05$) in one or more of the 11 flow conditions (grey) for the four different wind turbine layouts for simulations with Fitch and EWP. The colored areas show the locations of the different lease areas (see definitions in Figure 1). Note the NYBig (magenta) lease areas are only populated with wind turbines in the NYBIG simulations.

The large spatial extents of wakes from the LA clusters indicate there will be substantial and frequent array–array interactions. For example, if the ‘first-generation’ lease areas (i.e., those auctioned prior to February 2022) are occupied by 15 MW wind turbines installed with an ICD of 6 MWkm^{-2} , the ‘second-generation’ lease areas in NYBig are significantly

impacted by their wind farm wakes in multiple flow regimes (Figures 4 and 5). Further, for the NYBIG layout when the Fitch WFP is used there is no area south of Long Island that is not covered by the combined wind shadow from the existing LA (Figure 5). Indeed, in simulations of NYBIG with Fitch the area south of Long Island has an over 20% chance of being subject to a v_d of at least 5% at any given time (Figure 6). This probability is nearly twice that generated using output from EWP.

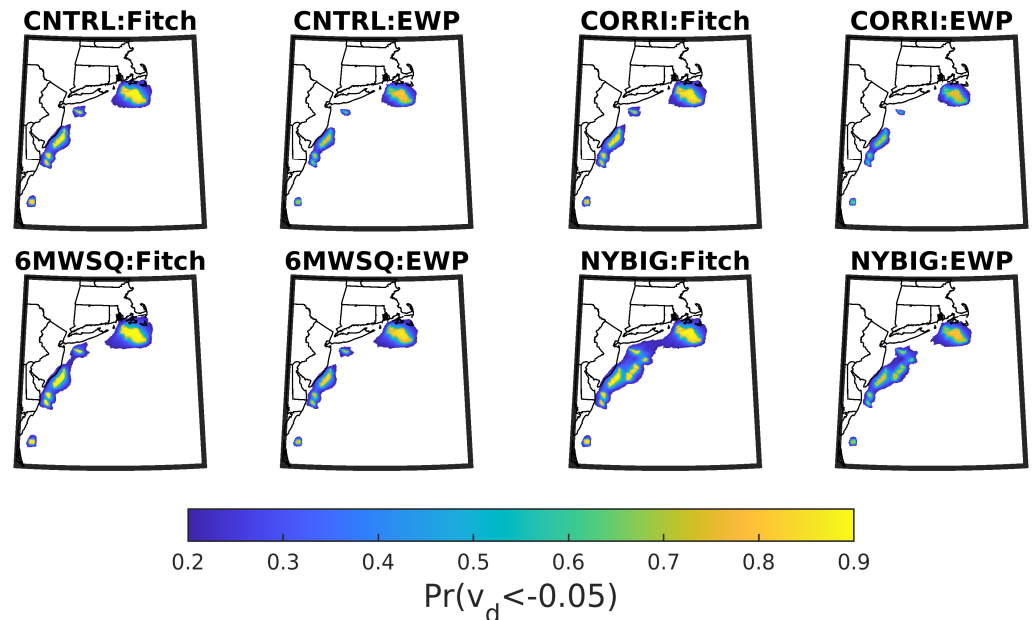


Figure 6. Marginal probability of experiencing $v_d \leq -0.05$ for the four different wind turbine layouts for simulations with Fitch and EWP.

Before discussing physical controls on wake extents computed using output from the two WFPs and building an emulator for NWE, it is important to acknowledge that in addition to the large number of grid cells that show evidence of wake effects (i.e., $\langle v_d \rangle < 0$), there are areas with $\langle v_d \rangle > 0$ for virtually all flow conditions (Figure 4). This implies that the presence of the wind turbines can lead to net wind speed increases, and this feature has also been observed in previous WRF perturbation studies [78,90]. While there is an induction (or blockage) effect as the flow approaches a large wind farm that leads to slight deceleration of the inflow and acceleration around the edges of the array in a bluff-body effect [65], a substantial fraction of the positive $\langle v_d \rangle$ are displaced from wind farm locations. Three primary reasons likely dominate the occurrence of $\langle v_d \rangle > 0$: (i) Flow disruption caused by the wind turbines in these large arrays may be of sufficient magnitude to change the atmospheric boundary layer in a way that causes large-scale differences in vertical momentum transport. Consistent with this thesis, grid cells exhibiting positive $\langle v_d \rangle$ are typically more numerous and the $\langle v_d \rangle$ are larger in simulations with higher numbers of wind turbines (6MWSQ and NYBIG) (e.g., compare panels for SW4–10: 1988-07-04, Figure 4f). (ii) Under low wind speed conditions, the normalization inherent in calculation of $\langle v_d \rangle$ may amplify differences in what are actually very similar wind speeds (e.g., SW4–10: 1988-07-04, Figure 4f). (iii) Numerical processes. For example, the rapid radiative transfer model (RRTM) and Duhia shortwave scheme used in these WRF simulations are computationally efficient and generally accurate [91,92] but RRTM uses a processor-local random number generator for some calculations which may lead to some differences in numerical solutions in d04 and d05 relative to d03.

3.3. NWE Physical Dependencies: Building an Emulator

The LA1–7 cluster is minimally impacted by distant wakes from the other lease areas except for the NYBIG simulation (Figures 5 and 6). Thus, we use output from this LA cluster to examine in detail the NWE for $v_d \leq -0.05$ as a function of prevailing meteorology, ICD and WFP. Cumulative wind farm wake extents (NWE) from individual model time steps do not always exhibit the expected behavior of increasing with ICD (Figure 7), due to the ‘deep array effect’ which means that some heavily waked wind turbines in the interior of arrays cease to operate in the higher ICD simulations (see following section). Nevertheless, as expected the average NWE increases with higher ICD. The mean NWE from LA1–7 for simulations with Fitch is 6% larger for the simulations with an ICD of 4.3 MWkm^{-2} versus 3.5 MWkm^{-2} . It is also 12% larger for an ICD of 6 MWkm^{-2} than 4.3 MWkm^{-2} . Equivalent values of the difference in NWE from EWP for CNTRL and 6MWSQ vs. CORRI are 9% and 16%. The ratio of mean NWE from Fitch and EWP for the three different ICDs (3.5 , 4.3 and 6.0 MWkm^{-2}) are 1.21, 1.18 and 1.13, respectively. Thus, NWE is consistently higher when computed using output from Fitch. The discrepancy between the NWE from the two WFPs declines in relative terms with increasing ICD.

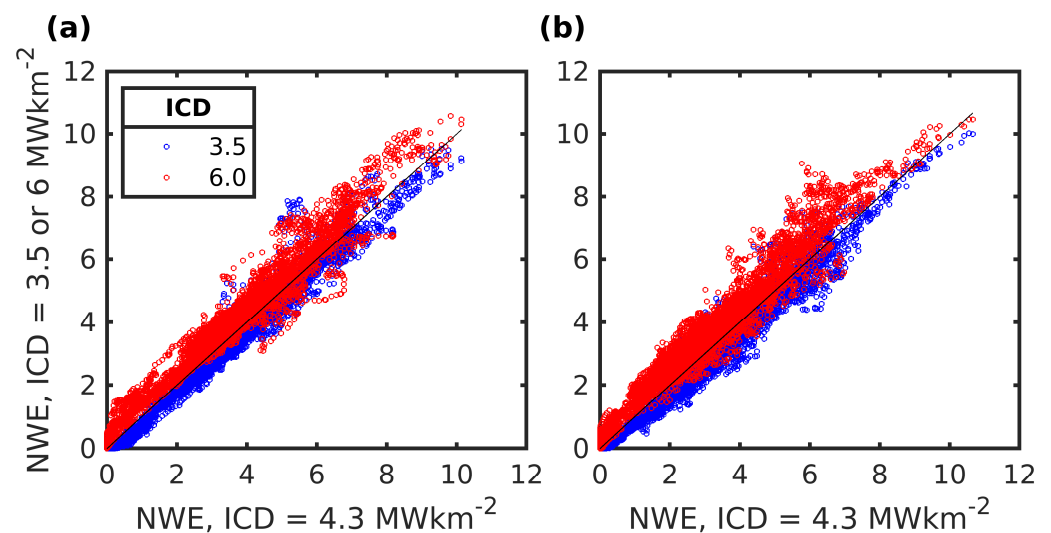


Figure 7. Scatterplots of 10 min values of normalized wake extent (NWE, for $v_d \leq -0.05$) based on output from all 11 5-day simulations from (a) Fitch and (b) EWP presented as a function of ICD, with values from the CNTRL layout (4.3 MWkm^{-2}) on the x-axis and values from the CORRI (3.5 MWkm^{-2}) and 6MWSQ (6 MWkm^{-2}) on the y-axis. The black solid line denotes 1:1 agreement.

To illustrate the physical dependencies of NWE and build a wake-extent emulator, three primary parameters are used as predictors of NWE in a regression analysis: (i) Wind speed, (ii) TKE and (iii) PBLH in the center of the LA1–7 cluster from d03 (freestream). The predictand is the mean NWE in output for ICD of 4.3 MWkm^{-2} (i.e., CNTRL). As described in the Materials and Methods, to enhance the stability of the model, data for each of the three predictors are sub-set into five percentile-based classes: 0–20th percentile, 20–40th percentile, etc., and then their joint occurrences are combined. Note that not all possible combinations have at least 10 members and so those combinations are excluded from the model construction, yielding 72 total classes in which the mean NWE from each wind farm parameterization (the predictand) and the mean values of the three predictors are derived (Figure 8).

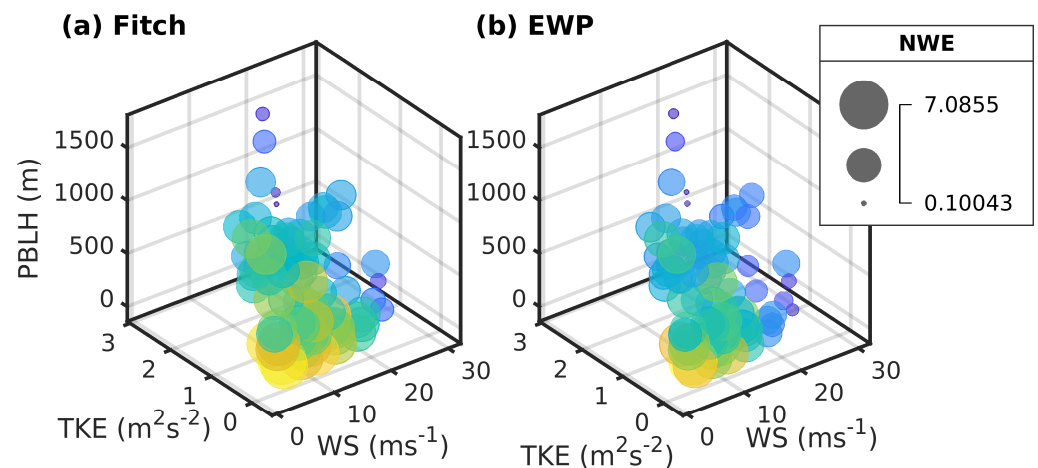


Figure 8. Bubbleplots of 10 min values of normalized wake extent (NWE, for $v_d \leq -0.05$) based on output from all 11 5-day simulations for CNTRL ($ICD = 4.3 \text{ MWkm}^{-2}$) from (a) Fitch and (b) EWP as a function of freestream wind speed (WS) and turbulent kinetic energy (TKE) at hub height and planetary boundary layer height (PBLH) at the centroid of the LA1–7 cluster. The full range of mean NWEs in each of the combined WS, TKE and PBLH classes is shown in the legend. The mean NWE in each class is coded both by the diameter of the bubble and the color from blue to yellow for low to high NWE.

The resulting stepwise linear regression models (forms as in Table 7) explain 85% of the variance in NWE. For both WFPs, the emulators indicate NWE decreases with increasing freestream hub-height wind speed, TKE and PBLH. The models are more complex for EWP. The stronger dependence of the NWE from EWP on wind speed implied by the stepwise regression is consistent with the dependence of both the energy extraction from the flow (as in Fitch) and the wake expansion via the eddy diffusion equation (EWP only) on the inflow wind speed. When the emulators are subject to re-specification using bootstrapping of the 72 predictor sets with replacement, all 1000 bootstrapped samples yield models with the same predictors as shown in Table 7.

Table 7. Coefficients in stepwise multiple linear regression equations where the normalized wake extent (NWE) is the predictand and the listed parameters are the freestream predictors. Note these models are conditioned on class mean values to enhance stability of the coefficients and using results from the CNTRL ($ICD = 4.3 \text{ MWkm}^{-2}$) experiment.

	Intercept	WS	TKE	PBLH	WS × TKE	WS ²	TKE ²	PBLH ²
Fitch ($R^2 = 0.85$)	6.1434	−0.0031	−0.8918	−0.0041	-	−0.0051	-	2.0406×10^{-6}
EWP ($R^2 = 0.85$)	6.8661	−0.1153	−1.4563	−0.0051	0.1706	−0.0051	−0.8977	2.6977×10^{-6}

These regression equations can be used as emulators and applied to output from any WRF simulation that uses the MYNN2.5 PBL scheme to make a first-order projection of the expected mean spatial extent of the wake from a prospective wind farm using only the modeled freestream time series of WS, TKE and PBLH. Naturally, care should be used in interpretation and out-of-sample implementation of these emulators, and it is important to recognize that the NWE is not solely a product of the time-synchronous wind speed at the center of the LA cluster. Nevertheless, when these equations are applied to the raw 10 min time series of freestream WS, TKE and PBLH from all 11, 5-day, simulations the results indicate the emulators reproduce the time series of NWE derived from the velocity deficits in each simulation period relatively well (Figure 9). Further, the mean NWE estimates from the velocity deficits and the emulator for Fitch (without frequency weighting) are 3.41 and 3.47, respectively, and equivalent NWE estimates from EWP are 2.89 and 2.96.

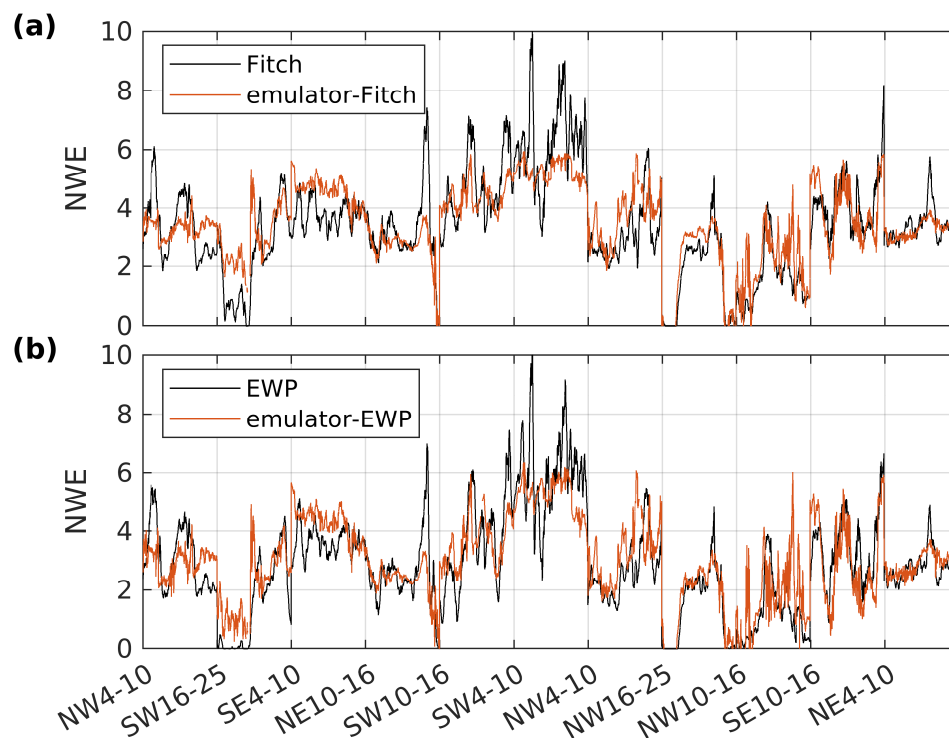


Figure 9. Normalized wake extent (NWE) for each 10 min time step when the freestream WS at the LA1–7 cluster centroid is >3 and <26 ms^{-1} , computed using the velocity deficit fields from simulations with (a) Fitch or (b) EWP and those generated by the emulators using the centroid freestream WS, TKE and PBLH (coefficients specified in Table 7). Labels on the x -axis indicate the start of each of the 11, 5-day, simulations and are ordered as in Table 3.

3.4. Deep Array Effect

As described above, the two WFPs differ markedly in terms of the way in which the wake is expanded and hence dissipated as it is advected downstream. This has implications not only for the probability that wakes will interact with downstream wind turbine arrays but also for the magnitude of the ‘deep array effect’ within very large offshore wind farms. Analyses of simulation output for the LA1–7 cluster that has a total area of 3675 km^2 for the four different layouts; CNTRL, CORRI, 6MWSQ and NYBIG, indicate that power output (and CF) from NYBIG and CNTRL are extremely similar for both wind farm parameterizations and all flow conditions (Table 5). This implies that the addition of new lease areas in New York Bight (located ~ 200 km to the southeast) has only a very minor influence on power production from the lease areas south of Massachusetts and Rhode Island. Thus, in the following we focus solely on output from wind turbines in LA1–7 for the following three wind farm layouts: CNTRL, CORRI and 6MWSQ, to quantify the presence and magnitude of the deep array effect.

In accordance with expectations, analyses of power production from 50 interior grid cells and 50 exterior grid cells for the LA1–7 cluster indicate evidence that the deep array effect is substantially enhanced for all flow conditions under the 6MWSQ layout for both WFPs (Figure 10a). For the 6MWSQ layout, interior wind turbines produce less than half the power of those in grid cells that experienced wind speeds closer to the freestream for all 11, 5-day, simulation periods. These analyses indicate the strongest deep array effect is manifest for the SW4–10: 1988-07-04 case. In this flow case for the 6MWSQ layout, power output from the interior grid cells is less than one-quarter of the ‘freestream power’ generated in exterior grid cells. During this same flow case, depending on the layout, analyses using the Fitch parameterization indicate wind turbines in the interior grid cells generate zero power during between 28% and 44% of the 10 min periods. This can be compared to 12% to 15% for wind turbines in the exterior grid cells (Figure 10b).

Equivalent results for the EWP are 28 to 38% for interior grid cells and 9 to 11% for the exterior grid cells.

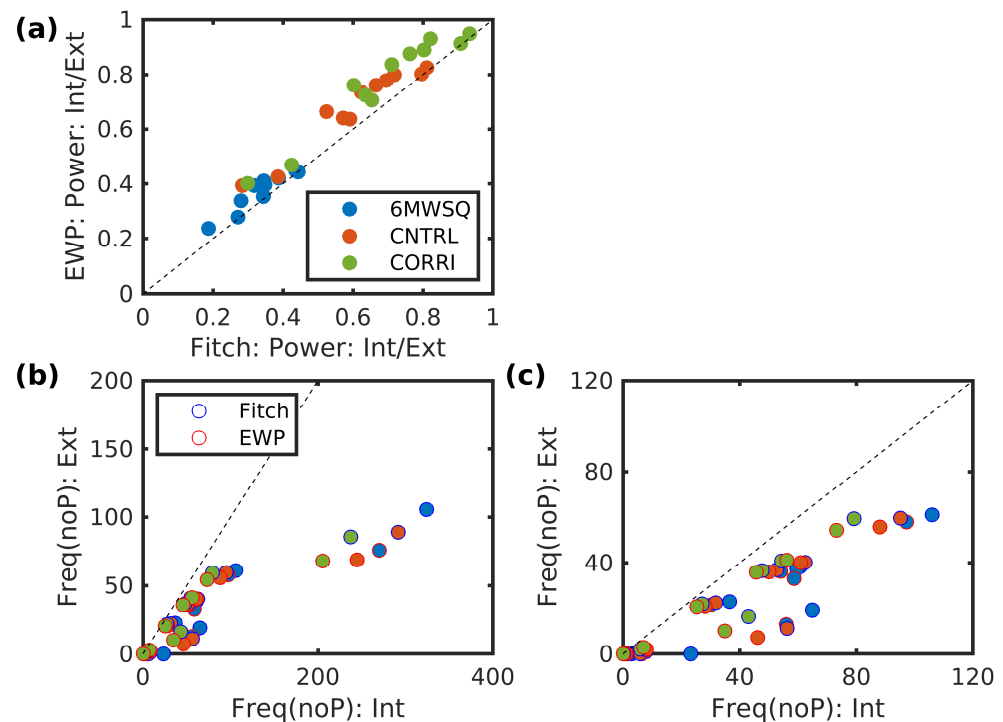


Figure 10. Scatterplots of the (a) ratio of mean power production from interior to exterior grid cells in LA1–7 based on simulations with Fitch and EWP of each flow condition for the three different layouts: CNTRL, CORRI and 6MWSQ. A ratio of 0.5 indicates that the mean power produced from the 50 interior grid cells (Int) is half of that from the exterior grid cells (Ext). The black line denotes the 1:1 equality. (b,c) Mean frequency (count of the 720 10 min periods in each flow case) with zero power for the 50 interior grid cells (Freq(noP): Int) and from the exterior grid cells (Freq(noP): Ext). The edge color denotes the wind farm parameterization, while the interior represents the layout (see legend in panel (a)). Note panel (c) shows the same data as panel (b) but is truncated to exclude the results for the SW4–10: 1988-07-04 case to allow close inspection of the other flow scenarios.

Although, as noted in the introduction, the WRF-WFPs are not optimized for representation of wakes internal to individual wind farms, these analyses indicate there is a substantial penalty in terms of power production and specifically a notable reduction in power from the interior of the LA1–7 cluster associated with use of the higher ICD. This effect would likely be disproportionately felt by the owner/operators of OCS-A 0501 and OCS-A 0520 since they are flanked by lease areas to both the west and the east. The frequency-weighted mean ratios of power from wind turbines in the interior and exterior grid cells are 0.56, 0.63 and 0.32 for the CNTRL, CORRI and 6MWSQ layouts based on analyses of output from the Fitch wind farm parameterization. Equivalent results for EWP are 0.64, 0.71 and 0.35. Thus, for the CNTRL layout the most heavily waked wind turbines generate only 56 to 64% of the power from the least-waked wind turbines. When the wind turbine spacing is decreased by 1 D (150 m) the ‘deep array effect’ is rendered considerably more intense and the power generation from the 50 worst-performing wind turbines is considerably reduced from 0.56 to 0.32 (Fitch) or 0.64 to 0.35 (EWP).

4. Discussion: Caveats

Simulation credibility for wind turbine wake extent, intensity and wake-induced power losses is dictated primarily by the fidelity with which the model reproduces key atmospheric features and power and wake generation by the wind turbines, plus the degree to which the simulated period(s) reflect the true geophysical conditions.

While the Fitch, EWP and other WFPs represent significant advances over early approaches based on enhanced surface roughness, none treats the near-wake characteristics in the same level of detail as can be achieved using microscale modeling and a more detailed treatment of the rotor. Also, wake superposition is better resolved in microscale models with finer grid resolution [35,90,93]. An early comparison of results from large eddy simulation (LES) and WRF with the Fitch wind farm parameterization for the Lillgrund wind farm under a single (uniform) flow field and neutral stability found over-estimation of power production within the wind farm was of a larger magnitude in the WRF simulations and the downstream wake recovery was faster in WRF [94]. Thus, it is plausible that the wake-induced power losses and normalized wake extents presented herein may underestimate those that would be projected in model studies using LES [95,96]. However, it is important to recall that the relative computational efficiency of models such as WRF means it is possible to sample a wider range of atmospheric conditions and build a more comprehensive climatology of wake characteristics than is currently possible with LES. As mentioned previously, only limited evaluation of the WRF-WFPs has been performed for offshore conditions and all pertain to much smaller wind turbine deployments than are currently being pursued along the U.S. east coast.

Differences between the wake extents and intensity from the two WRF-WFPs are to some degree insensitive to the precise atmospheric flow conditions sampled. However, the validity of results summarized herein with respect to projected power production, wake effects and power density variations with ICD are partly contingent on the degree to which the flow conditions sampled in the simulations reflect the true long-term wind climate. Based on output from d03 for all flow scenarios, the frequency-weighted mean wind speed close to the wind turbine hub height in the center of LA1–7 is 10.4 ms^{-1} , that for LA8 is 10.2 ms^{-1} , for LA9–13 it is 9.9 ms^{-1} and for LA14 and 15 it is 9.2 ms^{-1} (see Figure 3 inset). Mean wind speeds at a 10 m height based on observations with synthetic aperture radar and earlier WRF modeling indicate values of 7 to 7.5 ms^{-1} in the vicinity of LA1–7 [10]. Using a power law to extrapolate to a 143 m height with a coefficient of $1/7$ yields values of 10.3 to 11 ms^{-1} , and using a coefficient of 0.11, that was recommended for near-neutral stability over water surfaces [97], yields values of 9.4 to 10.1 ms^{-1} . These values thus bracket the frequency-weighted mean wind speed for this location in simulations presented herein (10.4 ms^{-1}). The mean hub-height value in LA1–7 from the NOW-23 WRF simulation data set [89] is also 10.4 ms^{-1} . However, lower mean wind speeds in the centers of LA8 and LA9–13 are indicated in the NOW-23 output of 9.7 and 9.6 ms^{-1} , respectively. These comparisons thus imply positive biases in mean wind speeds from the WRF simulations presented herein that are relatively small ($<0.5 \text{ ms}^{-1}$) and are likely the result of the selection of the flow cases to exclude wind speeds below the wind turbine cut-in when both power production and wake effects are zero. Under-sampling of very low wind speeds may have led to a small positive bias in CF reported herein.

Two-parameter Weibull distribution fits to the lidar observations and simulated wind speeds (both frequency-weighted to make them climatologically representative) indicate that the flow cases simulated herein generate relatively similar frequency distribution of wind speeds to those measured by the NY Mesonet lidars (Figure 11). However, the flow cases over-sample moderate wind speeds and under-sample wind speeds above those at which the IEA 15 MW reference wind turbine reaches rated capacity (approx. 11 ms^{-1} , see Figure 2). Comparison with almost two years of observations from the NYSERDA buoy-mounted lidars also suggests that the mean wind speeds at these two locations are slightly under-estimated in the WRF simulations presented herein by 0.2 ms^{-1} at E05 and almost 0.5 ms^{-1} at E06. Analyses of the wind roses from WRF and the offshore buoy-mounted lidars also indicate an over-sampling of northeasterly and northwesterly wind directions in the WRF simulations presented herein (Figure 12). However, it is important to recall that the buoy-mounted lidar data sets under-represent conditions from August through November [83].

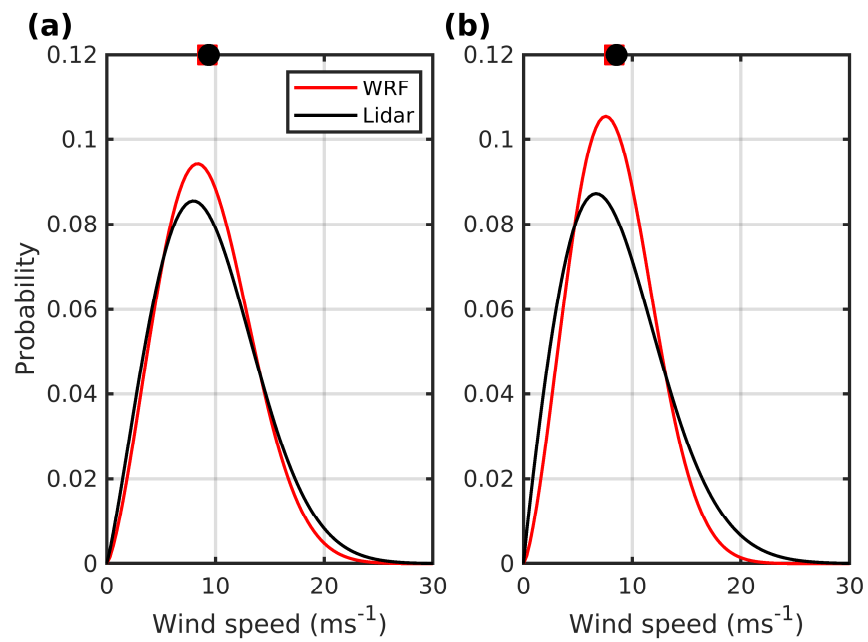


Figure 11. Two-parameter Weibull probability distributions fitted to the time series of wind speeds (lines), plus the mean wind speed at 150 m AGL (symbols) from the NY Mesonet lidar wind speeds and from the WRF model (143 m AGL) at (a) EHAM (40.970° N, −72.201° E) and (b) WANT (40.650° N, −73.505° E) on Long Island.

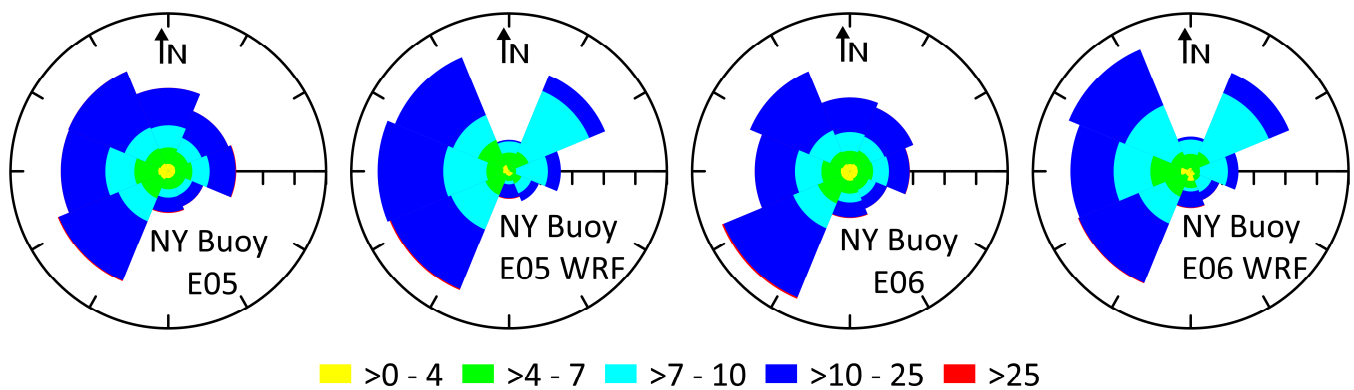


Figure 12. Wind roses summarizing the joint frequency of occurrence of flow in 45° wind direction sectors and the wind speed classes (ms^{−1}) shown in the legend for the two NYSERDA buoy-mounted lidars (140 m ASL) and the WRF output from d03 at ~143 m for those same locations. The radial tick-marks indicate frequency and are spaced at 5% increments to 25%.

These analyses thus suggest that the wind conditions sampled in the WRF wake simulations presented herein are broadly representative of those from long-term simulations and those from lidar campaigns. However, there are some discrepancies. The addition of further WRF wake simulations that sample additional flow conditions would certainly be beneficial.

The WRF model is subject to periodic updates and error corrections that influence the degree to which simulations performed with different model versions diverge. For example, mean CFs for the CNTRL layout derived using output from the Fitch parameterization in these new simulations with WRF v4.2.2 are lower than those generated in our previous research that employed WRF v3.8.1 [14] (Table 8). While a definitive cause of the differences cannot be unequivocally asserted, they likely reflect changes in the simulated wind field due to modifications in either/both the WRF pre-processing system and master code between WRF v3.8.1 and v4.2.2. A non-exhaustive list of these code changes as they relate

to the MYNN PBL scheme is given below based on WRF release documentation (<https://github.com/wrf-model/WRF/releases> (accessed on 1 November 2023) and <https://github.com/NCAR/WRFV3/releases> (accessed on 1 November 2023) and derived by comparing the appropriate user guides; available at https://www2.mmm.ucar.edu/wrf/users/docs/user_guide_V3/user_guide_V3.8/users_guide_chap5.htm (accessed on 1 November 2023) and https://www2.mmm.ucar.edu/wrf/users/docs/user_guide_v4/v4.2/users_guide_chap5.html) (accessed on 1 November 2023):

- Code correction in v4.1.3: ‘When using the MYNN PBL scheme, with `icloud_bl = 1` (which is default), restarts did not give bit-for-bit results when compared to a non-restart run. This has been a problem since the option was introduced in V3.8, but is now corrected.’
- Code correction in v4.1: ‘MYNN Updates: The biggest improvement is the reduction in the downward shortwave radiation bias through better cloud fraction and subgrid scale mixing ratios.’
- Default mixing length in MYNN in v3.8 was ‘RAP/HRRR (including BouLac in free atmosphere)’ (https://www2.mmm.ucar.edu/wrf/users/docs/user_guide_V3/user_guide_V3.8/users_guide_chap5.htm, accessed on 1 November 2023) but was changed by v4.2 to ‘experimental (includes cloud-specific mixing length and a scale-aware mixing length; following Ito et al. 2015, BLM); this option has been well-tested with the edmf options.’ (https://www2.mmm.ucar.edu/wrf/users/docs/user_guide_v4/v4.2/users_guide_chap5.html, accessed on 1 November 2023). In brief, Ito et al. [98] proposed a modification to the MYNN scheme wherein the mixing length scale is defined so that turbulence kinetic energy (TKE) dissipation is invariant with dx .

Table 8. Frequency-weighted mean CF (in %) from Fitch summarized by LA cluster based on the current simulations and those reported by Pryor et al. [14] for simulations with WRF v3.8.1.

Fitch	LA1–7	LA8	LA9–13	LA14 and 15
Pryor et al. [14] CNTRL (WRF v3.8.1)	46	56	45	40
CNTRL	43	52	43	40

The differences in freestream wind speeds between the two sets of simulations (those with v3.8.1 [14] and those presented here) are consistent with the strong dependence of simulated wind speeds on MYNN mixing length and are of a similar magnitude to those that have been reported from previous sensitivity analyses [99]. The differences in wind speeds at hub height on average are relatively small in most cases but exhibit substantial time variation both in magnitude and sign. For example, over the 5 days of the NW4–10 (1979-10-26 to 1979-10-30), the mean difference in WS at hub height (HH) in domain d02 (WRF v3.8.1 minus WRF v4.2.2), averaged in time and then in space, is -0.14 ms^{-1} . The equivalent difference in domain d03 is -0.10 ms^{-1} . For 10 of the 11 cases the absolute differences in WS at HH in domains d02 and d03 are $<0.4 \text{ ms}^{-1}$. For the 1981-08-29 case the differences are of larger magnitude and uniformly positive (i.e., the time-wise average WS at HH from WRF v3.8.1 is systematically higher than that from WRF v4.2.2). Accordingly, the difference in WS at HH over d03 averaged in time and then space is 0.94 ms^{-1} . The higher inflow WS in the prior simulations yielded higher CF (Table 8).

5. Conclusions

Global wind energy installations offshore increased to over 50 GW by the middle of 2022, and an additional 40 GW may be added by the end of 2025. Optimization of offshore wind farm location and design is increasingly becoming a three-scale process: (i) Identification of offshore areas suitable for wind turbine deployment (i.e., regional resource assessment), (ii) selection of specific lease areas for auction and development within that region and (iii) selection the exact layout and wind turbine for each wind farm [100].

The offshore wind energy deployments being developed along the U.S. east coast far exceed those that characterize existing offshore wind energy deployments and so are expected to experience greater wake losses. For example, the developments that are being undertaken in the offshore wind energy lease areas south of Massachusetts and Rhode Island cover a combined area of 3675 km² and will comprise between 13.5 and 22.3 GW of installed capacity (depending on the layout selected, see Table 2). This IC is five to eight times that of the combined Hornsea 1 and 2 projects. Hence, there is a need to advance understanding of, and predictive models of, power production plus wake production and propagation from these multi-GW installations.

Here we present new, climatologically representative simulations of meteorological conditions over offshore wind energy lease areas along the U.S. east coast, plus the likely electrical power production and wake-induced power losses from those prospective wind farms. The ensemble of simulations presented herein was performed with the Weather Research and Forecasting (WRF) model and is uniquely detailed relative to past research in that the simulations are climatologically representative (rather than case studies), cover the entirety of the U.S. east coast, include two wind farm parameterizations (Fitch and explicit wake parameterization (EWP)) and sample across four different wind turbine deployment scenarios and hence installed capacity densities.

The simulation output is used to quantify power production, wake generation and wake-induced power losses within large wind farm clusters and between these wind farms as a function of: (i) The installed capacity density (ICD; 3.5 to 6.0 MWkm⁻²), (ii) the wind farm parameterization and (iii) the version of WRF used. We further interrogate under what conditions the wind farm parameterizations yield different intra-array and inter-array wake losses and develop fast emulators of wake extents.

The fast emulators of wake extents indicate that over three-quarters of the variance in the spatial extent of the area covered by a velocity deficit of 5% (i.e., $\langle v_d \rangle < -0.05$) from the two WFPs is explained by linear dependencies on freestream wind speed, TKE and PBLH at the center of the lease area cluster. The emulators are demonstrated to be accurate and could be applied to output from any WRF simulation that employs the MYNN2.5 PBL scheme to make first-order estimates of the likelihood of wind farm interactions.

Mean system-wide capacity factors from the U.S. east coast lease areas considered range from 39–55% across the four layouts and two WFPs. If 15 MW wind turbines are deployed at a spacing of 1.85 km in all lease areas considered here, they are projected to provide 3.5 to 4.4% of U.S. national electricity demand. Although the largest cluster of lease areas considered covers 3675 km², the projections of wind power density (watts of electricity produced per square meter of lease area) increments across the range of ICD considered and lies between 2 and 3 Wm⁻², which implies that the scale of deployment considered here has not reached power production limits imposed by the rate of kinetic energy replacement.

Projected AEP and CFs from simulations presented herein indicate values higher than or comparable to smaller operating offshore wind farms in Europe. Nevertheless, these simulations also indicate that if all the lease areas considered are fully developed at ICDs of 3.5 to 6.0 MWkm⁻² there will be substantial array–array wake interactions and that those interactions will meaningfully reduce AEP from the individual lease area clusters. This finding implies there is value in system-wide coordination of both development of the existing lease areas and in consideration of wake effects when identifying potential new areas for auction [17]. However, guidance regarding potential wake losses is also shown to be critically contingent on the WFP used. As illustrated herein, power production efficiency differences from the two wind farm parameterizations are substantial and persist across all layouts considered. Use of EWP systematically leads to lower wake-induced power losses and hence substantially higher electricity production capacity factors (up to 10 percentage points larger in some lease area clusters) than the more commonly used Fitch parameterization. EWP systematically generates a weaker ‘deep array effect’ within a large wind farm cluster (3675 km²). If 15 MW wind turbines

are deployed at an ICD of 6 MWkm^{-2} the mean ratio of power generation from the lowest 50 power-producing wind turbines and the highest 50 power-producing wind turbines in this cluster is between 0.32 (Fitch) and 0.35 (EWP). That implies an intense ‘deep array effect’ and that the most heavily waked wind turbines will generate only 32–35% of the power of those that experience the freestream (undisturbed) flow. For the same meteorological conditions and an ICD of 3.5 MWkm^{-2} the equivalent power ratios are 0.56 and 0.64, from Fitch and EWP, respectively. This may indicate that to maximize system-wide power generation efficiency (CF) and minimize the LCoE, lower ICDs should be employed for these larger wind farm lease area clusters than typifies smaller operating European offshore wind farms.

EWP also generates weaker and more readily dissipated downstream wakes than Fitch irrespective of the specific atmospheric conditions and the wind turbine ICD and layout. For example, if the areal extent of the mean velocity deficit of 5% (i.e., $\langle v_d \rangle < -0.05$) is used as an index of the spatial extent of wind farm wakes, they are systematically larger for all layouts and all flow conditions in output from the Fitch wind farm parameterization. Sampling across all offshore wind energy lease areas considered here and the range of ICD, the whole wind farm wake extent is 1.18 to 1.38 times larger in simulations with Fitch. Given the rapidity of development of offshore wind energy IC there is an urgent need to move beyond model evaluation within the framework of case studies and for access to long-term experimental data (e.g., wind turbine SCADA and meteorological data from adjacent offshore wind farms) to permit rigorous evaluation of the wind farm parameterizations in order to establish best practice to guide future mesoscale wake modeling exercises with WRF.

Author Contributions: Conceptualization, S.C.P. and R.J.B.; methodology, S.C.P. and R.J.B.; software, S.C.P.; validation, S.C.P. and R.J.B.; formal analysis, S.C.P.; investigation, S.C.P.; resources, S.C.P.; data curation, S.C.P.; writing—original draft preparation, S.C.P.; writing—review and editing, S.C.P. and R.J.B.; visualization, S.C.P.; supervision, S.C.P.; project administration, S.C.P. and R.J.B.; funding acquisition, S.C.P. and R.J.B. All authors have read and agreed to the published version of the manuscript.

Funding: This research was funded primarily by the U.S. Department of Energy Office of Science (DE-SC0016605), with additional support from the Cornell Atkinson Center for Sustainability. This research was enabled by computational resources supported by the U.S. National Science Foundation via the Extreme Science and Engineering Discovery Environment (XSEDE) (award TG-ATM170024) and those of the National Energy Research Scientific Computing Center, a DOE Office of Science User Facility supported by the Office of Science of the U.S. Department of Energy under Contract No. DE-AC02-05CH11231. Original funding for the NYS Mesonet was provided by Federal Emergency Management Agency grant FEMA-4085-DR-NY, with the continued support of the NYS Division of Homeland Security & Emergency Services; the State of New York; the Research Foundation for the State University of New York (SUNY); the University at Albany; the Atmospheric Sciences Research Center (ASRC) at the University at Albany; and the Department of Atmospheric and Environmental Sciences (DAES) at the University at Albany. None of the funding agencies have reviewed information contained here and the opinions in this manuscript do not necessarily reflect those of any of these parties.

Data Availability Statement: Data from the NYSEDA Floating lidar buoy data in the New York Bight are provided by OceanTech Services/DNV under contract to NYSEDA and are available for download from: <https://oswbuoysny.resourcepanorama.dnv.com/> (accessed on 1 November 2023). The National Renewable Energy Laboratory, 2023 National Offshore Wind data set (NOW-23) is available from <https://dx.doi.org/10.25984/1821404> (accessed on 1 November 2023). Data from the New York State Mesonet can be requested from: <http://www.nysmesonet.org/> (accessed on 1 November 2023). Output from the WRF simulations is available upon reasonable request from the authors.

Acknowledgments: We gratefully acknowledge technical support from Tristan J. Shepherd, Andrea N. Hahmann and Oscar M. Garcia Santiago.

Conflicts of Interest: The authors declare no conflicts of interest.

References

1. Barthelmie, R.J.; Pryor, S.C. Climate Change Mitigation Potential of Wind Energy. *Climate* **2021**, *9*, 136. [CrossRef]
2. Rigano, J.P.; Delle Fave, A. Offshore wind: Government control and the regulatory landscape. *Environ. Claims J.* **2017**, *29*, 80–85. [CrossRef]
3. Global Wind Energy Council. *Global Wind Report 2023*; Global Wind Energy Council: Brussels, Belgium, 2023; p. 118. Available online: <https://gwec.net/gweecs-global-offshore-wind-report-2023/> (accessed on 1 November 2023).
4. Shields, M.; Stefek, J.; Oteri, F.; Kreider, M.; Gill, E.; Maniak, S.; Gould, R.; Malvik, C.; Tirone, S.; Hines, E. *A Supply Chain Road Map for Offshore Wind Energy in the United States*; National Renewable Energy Lab.(NREL): Golden, CO, USA, 2023. Available online: <https://www.osti.gov/biblio/1922189> (accessed on 1 November 2023).
5. Soares-Ramos, E.P.; de Oliveira-Assis, L.; Sarrias-Mena, R.; Fernández-Ramírez, L.M. Current status and future trends of offshore wind power in Europe. *Energy* **2020**, *202*, 117787. [CrossRef]
6. Sovacool, B.K.; Enevoldsen, P.; Koch, C.; Barthelmie, R.J. Cost performance and risk in the construction of offshore and onshore wind farms. *Wind Energy* **2017**, *20*, 891–908. [CrossRef]
7. Barthelmie, R.J.; Courtney, M.S.; Hojstrup, H.; Larsen, S.E. Meteorological aspects of offshore wind energy: Observations from the Vindeby wind farm. *J. Wind Eng. Ind. Aerodyn.* **1996**, *62*, 191–211. [CrossRef]
8. Jansen, M.; Staffell, I.; Kitzing, L.; Quoilin, S.; Wiggelinkhuizen, E.; Bulder, B.; Riepin, I.; Müsgens, F. Offshore wind competitiveness in mature markets without subsidy. *Nat. Energy* **2020**, *5*, 614–622. [CrossRef]
9. Diaz, H.; Soares, C.G. Review of the current status, technology and future trends of offshore wind farms. *Ocean Eng.* **2020**, *209*, 107381. [CrossRef]
10. Ahsbabs, T.; Maclaurin, G.; Draxl, C.; Jackson, C.; Monaldo, F.; Badger, M. US East Coast synthetic aperture radar wind atlas for offshore wind energy. *Wind Energy Sci.* **2020**, *5*, 1191–1210. [CrossRef]
11. Musial, W.; Heimiller, D.; Beiter, P.; Scott, G.; Draxl, C. *2016 Offshore Wind Energy Resource Assessment for the United States*; Technical Report NREL/TP-5000-66599; National Renewable Energy Laboratory: Golden, CO, USA, 2016; p. 88. Available online: <https://www.nrel.gov/docs/fy16osti/66599.pdf> (accessed on 16 July 2020).
12. Barthelmie, R.J.; Dantuono, K.; Renner, E.; Letson, F.; Pryor, S.C. Extreme wind and waves in U.S. east coast offshore wind energy lease areas. *Energies* **2021**, *14*, 1053. [CrossRef]
13. DeCastro, M.; Salvador, S.; Gómez-Gesteira, M.; Costoya, X.; Carvalho, D.; Sanz-Larruga, F.; Gimeno, L. Europe, China and the United States: Three different approaches to the development of offshore wind energy. *Renew. Sustain. Energy Rev.* **2019**, *109*, 55–70. [CrossRef]
14. Pryor, S.C.; Barthelmie, R.J.; Shepherd, T.J. Wind power production from very large offshore wind farms. *Joule* **2021**, *5*, 2663–2686. [CrossRef]
15. Mills, A.D.; Millstein, D.; Jeong, S.; Lavin, L.; Wiser, R.; Bolinger, M. Estimating the value of offshore wind along the United States' eastern coast. *Environ. Res. Lett.* **2018**, *13*, 09401310. [CrossRef]
16. Musial, W.; Spitsen, P.; Duffy, P.; Beiter, P.; Marquis, M.; Hammond, R.; Shields, M. *Offshore Wind Market Report: 2022 Edition*; USDOE Office of Energy Efficiency and Renewable Energy (EERE), Wind Energy Technologies Office (EE-4W); U.S. Department of Energy Office of Scientific and Technical Information: Oak Ridge, TN, USA, 2022. [CrossRef]
17. Pryor, S.C.; Barthelmie, R.J. Wind shadows impact planning of large offshore wind farms. *Appl. Energy* **2024**, *359*, 122755. [CrossRef]
18. Lundquist, J.; DuVivier, K.; Kaffine, D.; Tomaszewski, J. Costs and consequences of wind turbine wake effects arising from uncoordinated wind energy development. *Nat. Energy* **2019**, *4*, 26–34. [CrossRef]
19. Howland, M.F.; Quesada, J.B.; Martínez, J.J.P.; Larrañaga, F.P.; Yadav, N.; Chawla, J.S.; Sivaram, V.; Dabiri, J.O. Collective wind farm operation based on a predictive model increases utility-scale energy production. *Nat. Energy* **2022**, *7*, 818–827. [CrossRef]
20. Finserås, E.; Anchustegui, I.H.; Cheynet, E.; Gebhardt, C.G.; Reuder, J. Gone with the wind? Wind farm-induced wakes and regulatory gaps. *Mar. Policy* **2024**, *159*, 105897. [CrossRef]
21. Jansen, M.; Beiter, P.; Riepin, I.; Müsgens, F.; Guajardo-Fajardo, V.J.; Staffell, I.; Bulder, B.; Kitzing, L. Policy choices and outcomes for offshore wind auctions globally. *Energy Policy* **2022**, *167*, 113000. [CrossRef]
22. Johnston, B.; Foley, A.; Doran, J.; Littler, T. Levelised cost of energy, A challenge for offshore wind. *Renew. Energy* **2020**, *160*, 876–885. [CrossRef]
23. Caputo, A.C.; Federici, A.; Pelagagge, P.M.; Salini, P. Offshore wind power system economic evaluation framework under aleatory and epistemic uncertainty. *Appl. Energy* **2023**, *350*, 121585. [CrossRef]
24. Ioannou, A.; Angus, A.; Brennan, F. Stochastic financial appraisal of offshore wind farms. *Renew. Energy* **2020**, *145*, 1176–1191. [CrossRef]
25. Dukan, M.; Kitzing, L. The impact of auctions on financing conditions and cost of capital for wind energy projects. *Energy Policy* **2021**, *152*, 112197. [CrossRef]
26. Wind Europe. *Offshore Wind in Europe Key Trends and Statistics*; Wind Europe: Brussels, Belgium, 2020; p. 40. Available online: <https://windeurope.org/wp-content/uploads/files/about-wind/statistics/WindEurope-Annual-Offshore-Statistics-2019.pdf> (accessed on 27 February 2020).
27. Bosch, J.; Staffell, I.; Hawkes, A.D. Global levelised cost of electricity from offshore wind. *Energy* **2019**, *189*, 116357. [CrossRef]

28. Deutsche Wind Guard GmbH. *Capacity Densities of European Offshore Wind Farms*; Deutsche Wind Guard GmbH: Hamburg, Germany, 2018; p. 76. Available online: <https://www.msp-platform.eu/practices/capacity-densities-european-offshore-wind-farms> (accessed on 1 November 2023).
29. Barthelmie, R.J.; Hansen, K.S.; Pryor, S.C. Meteorological controls on wind turbine wakes. *Proc. IEEE* **2013**, *101*, 1010–1019. [[CrossRef](#)]
30. Barthelmie, R.J.; Jensen, L.E. Evaluation of wind farm efficiency and wind turbine wakes at the Nysted offshore wind farm. *Wind Energy* **2010**, *13*, 573–586. [[CrossRef](#)]
31. Thomsen, K.; Sørensen, P. Fatigue loads for wind turbines operating in wakes. *J. Wind Eng. Ind. Aerodyn.* **1999**, *80*, 121–136. [[CrossRef](#)]
32. Barthelmie, R.J.; Pryor, S.C.; Frandsen, S.T.; Hansen, K.; Schepers, J.G.; Rados, K.; Schlez, W.; Neubert, A.; Jensen, L.E.; Neckelmann, S. Quantifying the impact of wind turbine wakes on power output at offshore wind farms. *J. Atmos. Ocean. Technol.* **2010**, *27*, 1302–1317. [[CrossRef](#)]
33. Hasager, C.B.; Vincent, P.; Badger, J.; Badger, M.; Di Bella, A.; Peña, A.; Husson, R.; Volker, P.J. Using satellite SAR to characterize the wind flow around offshore wind farms. *Energies* **2015**, *8*, 5413–5439. [[CrossRef](#)]
34. Pryor, S.C.; Shepherd, T.J.; Volker, P.; Hahmann, A.N.; Barthelmie, R.J. ‘Wind theft’ from onshore wind turbine arrays: Sensitivity to wind farm parameterization and resolution. *J. Appl. Meteorol. Climatol.* **2020**, *59*, 153–174. [[CrossRef](#)]
35. Wu, Y.-T.; Porté-Agel, F. Atmospheric turbulence effects on wind-turbine wakes: An LES study. *Energies* **2012**, *5*, 5340–5362. [[CrossRef](#)]
36. Lee, J.C.; Lundquist, J.K. Observing and simulating wind-turbine wakes during the evening transition. *Bound.-Layer Meteorol.* **2017**, *164*, 449–474. [[CrossRef](#)]
37. Enevoldsen, P.; Valentine, S.V. Do onshore and offshore wind farm development patterns differ? *Energy Sustain. Dev.* **2016**, *35*, 41–51. [[CrossRef](#)]
38. Enevoldsen, P.; Xydis, G. Examining the trends of 35 years growth of key wind turbine components. *Energy Sustain. Dev.* **2019**, *50*, 18–26. [[CrossRef](#)]
39. Sickler, M.; Ummels, B.; Zaaier, M.; Schmehl, R.; Dykes, K. Offshore wind farm optimisation: A comparison of performance between regular and irregular wind turbine layouts. *Wind Energy Sci.* **2023**, *8*, 1225–1233. [[CrossRef](#)]
40. Bensason, D.; Simley, E.; Roberts, O.; Fleming, P.; Debnath, M.; King, J.; Bay, C.; Mudafort, R. Evaluation of the potential for wake steering for US land-based wind power plants. *J. Renew. Sustain. Energy* **2021**, *13*, 033303. [[CrossRef](#)]
41. Staid, A.; VerHulst, C.; Guikema, S.D. A comparison of methods for assessing power output in non-uniform onshore wind farms. *Wind Energy* **2018**, *21*, 42–52. [[CrossRef](#)]
42. Doekemeijer, B.M.; Simley, E.; Fleming, P. Comparison of the Gaussian wind farm model with historical data of three offshore wind farms. *Energies* **2022**, *15*, 1964. [[CrossRef](#)]
43. Ali, K.; Schultz, D.M.; Revell, A.; Stallard, T.; Ouro, P. Assessment of five wind-farm parameterizations in the Weather Research and Forecasting model: A case study of wind farms in the North Sea. *Mon. Weather Rev.* **2023**, *151*, 2333–2359. [[CrossRef](#)]
44. Xie, B.; Fung, J.C.; Chan, A.; Lau, A. Evaluation of nonlocal and local planetary boundary layer schemes in the WRF model. *J. Geophys. Res. Atmos.* **2012**, *117*, D12103. [[CrossRef](#)]
45. Peña, A.; Hahmann, A.N. Atmospheric stability and turbulence fluxes at Horns Rev—An intercomparison of sonic, bulk and WRF model data. *Wind Energy* **2012**, *15*, 717–731. [[CrossRef](#)]
46. Stevens, R.J.; Meneveau, C. Flow structure and turbulence in wind farms. *Annu. Rev. Fluid Mech.* **2017**, *49*, 311–339. [[CrossRef](#)]
47. Miller, L.M.; Brunzell, N.A.; Mechem, D.B.; Gans, F.; Monaghan, A.J.; Vautard, R.; Keith, D.W.; Kleidon, A. Two methods for estimating limits to large-scale wind power generation. *Proc. Natl. Acad. Sci. USA* **2015**, *112*, 11169–11174. [[CrossRef](#)] [[PubMed](#)]
48. Volker, P.J.H.; Hahmann, A.N.; Badger, J.; Jørgensen, H.E. Prospects for generating electricity by large onshore and offshore wind farms. *Environ. Res. Lett.* **2017**, *12*, 034022. [[CrossRef](#)]
49. Christiansen, M.B.; Hasager, C. Wake effects of large offshore wind farms identified from satellite SAR. *Remote Sens. Environ.* **2005**, *98*, 251–268. [[CrossRef](#)]
50. Eriksson, O.; Mikkelsen, R.; Hansen, K.S.; Nilsson, K.; Ivanell, S. Analysis of long distance wakes of Horns Rev I using actuator disc approach. *J. Phys. Conf. Ser.* **2014**, *555*, 012032. [[CrossRef](#)]
51. Ahsbals, T.; Nygaard, N.G.; Newcombe, A.; Badger, M. Wind farm wakes from SAR and doppler radar. *Remote Sens.* **2020**, *12*, 462. [[CrossRef](#)]
52. Nygaard, N.G.; Newcombe, A.C. Wake behind an offshore wind farm observed with dual-Doppler radars. *J. Phys. Conf. Ser.* **2018**, *1037*, 072008. [[CrossRef](#)]
53. Cañadillas, B.; Beckenbauer, M.; Trujillo, J.J.; Dörenkämper, M.; Foreman, R.; Neumann, T.; Lampert, A. Offshore wind farm cluster wakes as observed by long-range-scanning wind lidar measurements and mesoscale modeling. *Wind Energy Sci.* **2022**, *7*, 1241–1262. [[CrossRef](#)]
54. Platis, A.; Siedersleben, S.K.; Bange, J.; Lampert, A.; Bärfuss, K.; Hankers, R.; Cañadillas, B.; Foreman, R.; Schulz-Stellenfleth, J.; Djath, B.; et al. First in situ evidence of wakes in the far field behind offshore wind farms. *Sci. Rep.* **2018**, *8*, 2163. [[CrossRef](#)]
55. Cañadillas, B.; Foreman, R.; Barth, V.; Siedersleben, S.; Lampert, A.; Platis, A.; Djath, B.; Schulz-Stellenfleth, J.; Bange, J.; Emeis, S. Offshore wind farm wake recovery: Airborne measurements and its representation in engineering models. *Wind Energy* **2020**, *23*, 1249–1265. [[CrossRef](#)]

56. Fischereit, J.; Brown, R.; Larsén, X.G.; Badger, J.; Hawkes, G. Review of Mesoscale Wind-Farm Parametrizations and Their Applications. *Bound.-Layer Meteorol.* **2022**, *182*, 175–224. [[CrossRef](#)]
57. Cuevas-Figueroa, G.; Stansby, P.K.; Stallard, T. Accuracy of WRF for prediction of operational wind farm data and assessment of influence of upwind farms on power production. *Energy* **2022**, *254*, 124362. [[CrossRef](#)]
58. Hahmann, A.N.; Sile, T.; Witha, B.; Davis, N.N.; Dörenkämper, M.; Ezber, Y.; García-Bustamante, E.; González Rouco, J.F.; Navarro, J.; Olsen, B.T.; et al. The Making of the New European Wind Atlas, Part 1: Model Sensitivity. *Geosci. Model Dev.* **2020**, *13*, 5053–5078. [[CrossRef](#)]
59. Pryor, S.C.; Coburn, J.J.; Barthelmie, R.J.; Shepherd, T.J. Projecting Future Energy Production from Operating Wind Farms in North America: Part 1: Dynamical Downscaling. *J. Appl. Meteorol. Climatol.* **2022**, *62*, 63–80. [[CrossRef](#)]
60. Losada Carreño, I.; Craig, M.T.; Rossol, M.; Ashfaq, M.; Batibeniz, F.; Haupt, S.E.; Draxl, C.; Hodge, B.-M.; Brancucci, C. Potential impacts of climate change on wind and solar electricity generation in Texas. *Clim. Chang.* **2020**, *163*, 745–766. [[CrossRef](#)]
61. Xu, W.; Liu, P.; Cheng, L.; Zhou, Y.; Xia, Q.; Gong, Y.; Liu, Y. Multi-step wind speed prediction by combining a WRF simulation and an error correction strategy. *Renew. Energy* **2021**, *163*, 772–782. [[CrossRef](#)]
62. Xing, Y.; Lien, F.-S.; Melek, W.; Yee, E. A Multi-Hour Ahead Wind Power Forecasting System Based on a WRF-TOPSIS-ANFIS Model. *Energies* **2022**, *15*, 5472. [[CrossRef](#)]
63. Haupt, S.E.; McCandless, T.C.; Dettling, S.; Alessandrini, S.; Lee, J.A.; Linden, S.; Petzke, W.; Brummet, T.; Nguyen, N.; Kosović, B. Combining artificial intelligence with physics-based methods for probabilistic renewable energy forecasting. *Energies* **2020**, *13*, 1979. [[CrossRef](#)]
64. Fitch, A.C.; Olson, J.B.; Lundquist, J.K.; Dudhia, J.; Gupta, A.K.; Michalakes, J.; Barstad, I. Local and Mesoscale Impacts of Wind Farms as Parameterized in a Mesoscale NWP Model. *Mon. Weather Rev.* **2012**, *140*, 3017–3038. [[CrossRef](#)]
65. Volker, P.J.H.; Badger, J.; Hahmann, A.N.; Ott, S. The Explicit Wake Parametrisation V1.0: A wind farm parametrisation in the mesoscale model WRF. *Geosci. Model Dev.* **2015**, *8*, 3481–3522. [[CrossRef](#)]
66. Archer, C.L.; Wu, S.; Ma, Y.; Jiménez, P.A. Two corrections for turbulent kinetic energy generated by wind farms in the WRF model. *Mon. Weather Rev.* **2020**, *148*, 4823–4835. [[CrossRef](#)]
67. Shepherd, T.J.; Barthelmie, R.J.; Pryor, S.C. Sensitivity of wind turbine array downstream effects to the parameterization used in WRF. *J. Appl. Meteorol. Climatol.* **2020**, *59*, 333–361. [[CrossRef](#)]
68. Pryor, S.C.; Shepherd, T.; Volker, P.; Hahmann, A.; Barthelmie, R.J. Diagnosing systematic differences in predicted wind turbine array-array interactions. *J. Phys. Conf. Series. Sci. Mak. Torque Wind.* **2020**, *1618*, 062023. [[CrossRef](#)]
69. Siedersleben, S.K.; Platis, A.; Lundquist, J.K.; Djath, B.; Lampert, A.; Bärfuss, K.; Canadillas, B.; Schultz-Stellenfleth, J.; Bange, J.; Neumann, T.; et al. Observed and simulated turbulent kinetic energy (WRF 3.8.1) overlarge offshore wind farms. *Geosci. Model Dev.* **2020**, *13*, 249–268. [[CrossRef](#)]
70. Larsén, X.G.; Fischereit, J. A case study of wind farm effects using two wake parameterizations in the Weather Research and Forecasting (WRF) model (V3. 7.1) in the presence of low-level jets. *Geosci. Model Dev.* **2021**, *14*, 3141–3158. [[CrossRef](#)]
71. Garcia-Santiago, O.M.; Badger, J.; Hahmann, A.N.; da Costa, G.L. Evaluation of two mesoscale wind farm parametrizations with offshore tall masts. *J. Phys. Conf. Ser.* **2022**, *2265*, 022038. [[CrossRef](#)]
72. Fischereit, J.; Schaldemose Hansen, K.; Larsén, X.G.; van der Laan, M.P.; Réthoré, P.-E.; Murcia Leon, J.P. Comparing and validating intra-farm and farm-to-farm wakes across different mesoscale and high-resolution wake models. *Wind Energy Sci.* **2022**, *7*, 1069–1091. [[CrossRef](#)]
73. Rybchuk, A.; Juliano, T.W.; Lundquist, J.K.; Rosencrans, D.; Bodini, N.; Optis, M. The sensitivity of the fitch wind farm parameterization to a three-dimensional planetary boundary layer scheme. *Wind Energy Sci.* **2022**, *7*, 2085–2098. [[CrossRef](#)]
74. Bureau of Ocean Energy Management. *Outer Continental Shelf: Renewable Energy Leases Map Book*; U.S. Department of the Interior: Bureau of Ocean Energy Management: Sterling, VA, USA, 2022; p. 33. Available online: <https://www.boem.gov/renewable-energy/mapping-and-data/renewable-energy-gis-data> (accessed on 1 November 2023).
75. Schneemann, J.; Rott, A.; Dörenkämper, M.; Steinfeld, G.; Kühn, M. Cluster wakes impact on a far-distant offshore wind farm's power. *Wind Energy Sci.* **2020**, *5*, 29–49. [[CrossRef](#)]
76. Mlawer, E.J.; Taubman, S.J.; Brown, P.D.; Iacono, M.J.; Clough, S.A. Radiative transfer for inhomogeneous atmospheres: RRTM, a validated correlated-k model for the longwave. *J. Geophys. Res. Atmos.* **1997**, *102*, 16663–16682. [[CrossRef](#)]
77. Dudhia, J. Numerical study of convection observed during the winter monsoon experiment using a mesoscale two-dimensional model. *J. Atmos. Sci.* **1989**, *46*, 3077–3107. [[CrossRef](#)]
78. Ferrier, B.S.; Jin, Y.; Lin, Y.; Black, T.; Rogers, E.; DiMego, G. Implementation of a new grid-scale cloud and precipitation scheme in the NCEP Eta model. In Proceedings of the 15th Conference on Numerical Weather Prediction, San Antonio, TX, USA, 12–16 August 2002; pp. 280–283.
79. Kain, J.S. The Kain–Fritsch convective parameterization: An update. *J. Appl. Meteorol.* **2004**, *43*, 170–181. [[CrossRef](#)]
80. Beljaars, A. The parametrization of surface fluxes in large-scale models under free convection. *Q. J. R. Meteorol. Soc.* **1995**, *121*, 255–270.
81. Tewari, M.; Chen, F.; Wang, W.; Dudhia, J.; LeMone, M.; Mitchell, K.; Ek, M.; Gayno, G.; Wegiel, J.; Cuenca, R. Implementation and verification of the unified NOAH land surface model in the WRF model. In Proceedings of the 20th Conference on Weather Analysis and Forecasting/16th Conference on Numerical Weather Prediction, Seattle, WA, USA, 12–16 January 2004; Volume 1115. Available online: https://ams.confex.com/ams/84Annual/techprogram/paper_69061.htm (accessed on 1 November 2023).

82. Nakanishi, M.; Niino, H. An improved Mellor–Yamada level-3 model: Its numerical stability and application to a regional prediction of advection fog. *Bound.-Layer Meteorol.* **2006**, *119*, 397–407. [[CrossRef](#)]
83. Foody, R.; Coburn, J.; Aird, J.A.; Barthelmie, R.J.; Pryor, S.C. Onshore and Offshore Wind Resources and Operating Conditions in the Eastern US. *Wind Energy Sci.* **2024**, *9*, 263–280. [[CrossRef](#)]
84. Agora Engiewende; Agora Verkehrswende; Technical University of Denmark; Max-Planck-Institute for Biogeochemistry. *Making the Most of Offshore Wind: Re-Evaluating the Potential of Offshore Wind in the German North Sea*; 36-2020-EN; Agora Energiewende: Berlin, Germany, 2020; p. 80. Available online: <https://www.agora-energiewende.de/en/publications/making-the-most-of-offshore-wind> (accessed on 1 November 2023).
85. Gaertner, E.; Rinker, J.; Sethuraman, L.; Zahle, F.; Anderson, B.; Barter, G.E.; Abbas, N.J.; Meng, F.; Bortolotti, P.; Skrzypinski, W. *IEA Wind TCP Task 37: Definition of the IEA 15-Megawatt Offshore Reference Wind Turbine*; National Renewable Energy Lab.(NREL): Golden, CO, USA, 2020; p. 44. Available online: <https://www.osti.gov/biblio/1603478> (accessed on 1 November 2023).
86. Hersbach, H.; Bell, B.; Berrisford, P.; Hirahara, S.; Horányi, A.; Muñoz-Sabater, J.; Nicolas, J.; Peubey, C.; Radu, R.; Schepers, D.; et al. The ERA5 global reanalysis. *Q. J. R. Meteorol. Soc.* **2020**, *146*, 1999–2049. [[CrossRef](#)]
87. Wilks, D.S. *Statistical Methods in the Atmospheric Sciences*; Academic Press: Oxford, UK, 2011; Volume 100, ISBN 9780123850225.
88. Debnath, M.; Doubrawa, P.; Optis, M.; Hawbecker, P.; Bodini, N. Extreme wind shear events in US offshore wind energy areas and the role of induced stratification. *Wind Energy Sci.* **2021**, *6*, 1043–1059. [[CrossRef](#)]
89. National Renewable Energy Laboratory. *2023 National Offshore Wind Data Set (NOW-23)*; National Renewable Energy Laboratory: Golden, CO, USA, 2020. [[CrossRef](#)]
90. Wu, Y.-T.; Porté-Agel, F. Simulation of Turbulent Flow Inside and Above Wind Farms: Model Validation and Layout Effects. *Bound.-Layer Meteorol.* **2013**, *146*, 181–205. [[CrossRef](#)]
91. Ruiz-Arias, J.A.; Dudhia, J.; Santos-Alamillos, F.J.; Pozo-Vázquez, D. Surface clear-sky shortwave radiative closure intercomparisons in the Weather Research and Forecasting model. *J. Geophys. Res. Atmos.* **2013**, *118*, 9901–9913. [[CrossRef](#)]
92. Mooney, P.; Mulligan, F.; Fealy, R. Evaluation of the sensitivity of the weather research and forecasting model to parameterization schemes for regional climates of Europe over the period 1990–1995. *J. Clim.* **2013**, *26*, 1002–1017. [[CrossRef](#)]
93. Ma, Y.; Archer, C.L.; Vassel-Be-Hagh, A. Comparison of individual versus ensemble wind farm parameterizations inclusive of sub-grid wakes for the WRF model. *Wind Energy* **2022**, *25*, 1573–1595. [[CrossRef](#)]
94. Eriksson, O.; Lindvall, J.; Breton, S.-P.; Ivanell, S. Wake downstream of the Lillgrund wind farm-A Comparison between LES using the actuator disc method and a wind farm parametrization in WRF. *J. Phys. Conf. Ser.* **2015**, *625*, 012028. [[CrossRef](#)]
95. Sood, I.; Simon, E.; Vitsas, A.; Blockmans, B.; Larsen, G.C.; Meyers, J. Comparison of large eddy simulations against measurements from the Lillgrund offshore wind farm. *Wind Energy Sci.* **2022**, *7*, 2469–2489. [[CrossRef](#)]
96. Maas, O.; Raasch, S. Wake properties and power output of very large wind farms for different meteorological conditions and turbine spacings: A large-eddy simulation case study for the German Bight. *Wind Energy Sci.* **2022**, *7*, 715–739. [[CrossRef](#)]
97. Hsu, S.A.; Meindl, E.A.; Gilhousen, D.B. Determining the power-law wind-profile exponent under near-neutral stability conditions at sea. *J. Appl. Meteorol.* **1994**, *33*, 757–765. [[CrossRef](#)]
98. Ito, J.; Niino, H.; Nakanishi, M.; Moeng, C.-H. An extension of the Mellor–Yamada model to the terra incognita zone for dry convective mixed layers in the free convection regime. *Bound.-Layer Meteorol.* **2015**, *157*, 23–43. [[CrossRef](#)]
99. Yang, B.; Berg, L.K.; Qian, Y.; Wang, C.; Hou, Z.; Liu, Y.; Shin, H.H.; Hong, S.; Pekour, M. Parametric and structural sensitivities of turbine-height wind speeds in the boundary layer parameterizations in the weather research and forecasting model. *J. Geophys. Res. Atmos.* **2019**, *124*, 5951–5969. [[CrossRef](#)]
100. Cazzaro, D.; Trivella, A.; Corman, F.; Pisinger, D. Multi-scale optimization of the design of offshore wind farms. *Appl. Energy* **2022**, *314*, 118830. [[CrossRef](#)]

Disclaimer/Publisher’s Note: The statements, opinions and data contained in all publications are solely those of the individual author(s) and contributor(s) and not of MDPI and/or the editor(s). MDPI and/or the editor(s) disclaim responsibility for any injury to people or property resulting from any ideas, methods, instructions or products referred to in the content.